

# Unsupervised learning of spatially varying regularization for diffeomorphic image registration

Junyu Chen<sup>a,\*</sup>, Shuwen Wei<sup>b</sup>, Yihao Liu<sup>c</sup>, Zhangxing Bian<sup>b</sup>, Yufan He<sup>d</sup>, Aaron Carass<sup>b</sup>, Harrison Bai<sup>a</sup>, Yong Du<sup>a</sup>

<sup>a</sup>Department of Radiology and Radiological Science, Johns Hopkins School of Medicine, MD, USA

<sup>b</sup>Image Analysis and Communications Laboratory, Department of Electrical and Computer Engineering, Johns Hopkins University, MD, USA

<sup>c</sup>Department of Electrical and Computer Engineering, Vanderbilt University, TN, USA

<sup>d</sup>NVIDIA Corporation, Bethesda, MD, USA

## ARTICLE INFO

Article history:

Received xxxx

Received in final form xxxx

Accepted xxxx

Available online xxxx

Communicated by xxxx

**Keywords:** Deformable Image Registration, Deep Neural Networks, Spatially Varying Regularization

## ABSTRACT

Spatially varying regularization accommodates the deformation variations that may be necessary for different anatomical regions during deformable image registration. Historically, optimization-based registration models have harnessed spatially varying regularization to address anatomical subtleties. However, most modern deep learning-based models tend to gravitate towards spatially invariant regularization, wherein a homogeneous regularization strength is applied across the entire image, potentially disregarding localized variations. In this paper, we propose a hierarchical probabilistic model that integrates a prior distribution on the deformation regularization strength, enabling the end-to-end learning of a spatially varying deformation regularizer directly from the data. The proposed method is straightforward to implement and easily integrates with various registration network architectures. Additionally, automatic tuning of hyperparameters is achieved through Bayesian optimization, allowing efficient identification of optimal hyperparameters for any given registration task. Comprehensive evaluations on publicly available datasets demonstrate that the proposed method significantly improves registration performance and enhances the interpretability of deep learning-based registration, all while maintaining smooth deformations.

## 1. Introduction

Deformable image registration (DIR) is an important component in many medical imaging applications. The objective is to estimate a smooth deformation that aligns a moving image with a fixed image to maximize their similarity. Optimization-based DIR methods, such as LDDMM (Beg et al., 2005), SyN (Avants et al., 2008), Demons (Thirion, 1998; Vercauteren et al., 2009), and FLASH (Zhang and Fletcher, 2019), are built on rigorous mathematical frameworks and have traditionally been the preferred methods for accomplishing DIR tasks. However, these methods present certain limitations: they often require time-consuming optimization steps, and their instance-specific optimization scheme makes it challenging to integrate auxiliary or prior information into the registration process.

In recent years, the advancement of deep neural networks (DNNs) and their success in processing image data have sparked increased interest in developing DNN-based methods for medical image registration. Deep learning-based registration methods train a DNN on an image dataset to optimize a global

objective function, usually in the form of a similarity measure, with a regularizer added to enforce the spatial smoothness of the deformation. Such methods circumvent the laborious iterative optimization procedure, enabling faster and sometimes superior deformation mappings in a fraction of the time required by traditional methods. For a comprehensive review of recent developments in deep learning-based medical image registration, the readers are directed to (Chen et al., 2025). In the remainder of the paper, we use the terms "learning-based methods" to denote "deep learning-based methods" for ease of discussion.

In learning-based DIR, most existing methods adopt the objective function of traditional methods to serve as loss functions for training DNNs. Mathematically, this is expressed as:

$$\mathcal{E}(\mathbf{m} \circ \phi, \mathbf{f}) + \lambda \mathcal{R}(\phi), \quad (1)$$

where  $\phi$  is a deformation field, the first term,  $\mathcal{E}(\mathbf{m} \circ \phi, \mathbf{f})$ , is a similarity metric between the deformed moving image, denoted as  $\mathbf{m} \circ \phi$ , and the fixed image  $\mathbf{f}$ . The term  $\mathcal{R}(\phi)$  acts as a regularizer that encourages the spatial smoothness of the deformation field  $\phi$ . The hyperparameter  $\lambda$  controls the degree of regularization and is often designated as a constant and *spatially-invariant* value (Balakrishnan et al., 2019; Dalca et al., 2019b; de Vos

\*Corresponding author. E-mail address: jchen245@jhmi.edu.

et al., 2017; Chen et al., 2021a, 2022b; Liu et al., 2022a; Kim et al., 2021; Liu et al., 2024b; Chen et al., 2025). However, employing a constant regularization strength assumes that all data necessitate a similar level of regularization, neglecting the possibility that optimal regularization could vary based on the particular images at hand. For example, the anatomical structure of an individual may better resemble certain individuals than others (Simpson et al., 2012). As such, a constant regularization strategy might not always be the most effective. To address this, some methods have been proposed to condition  $\lambda$  within the DNN framework, allowing for the adjustment of the regularization strength during the test time (Mok and Chung, 2021; Hoopes et al., 2021). Although this offers a degree of adaptability, the challenge of determining the optimal regularization strength for the given image still persists. Additionally, these works applied a *spatially-invariant* regularization strength to the entire image, which does not account for the variations of deformation that may be necessary for different regions of the image (Niethammer et al., 2019). An example of this can be seen in brain scan registration, where the brain ventricles can vary in size between different patients, leading to different scales of deformation in the ventricles compared to other parts of the brain (Niethammer et al., 2019). Similarly, when inhale-to-exhale images of the lung are aligned, larger lung deformations are anticipated than those of surrounding tissue (Shen et al., 2019). Furthermore, less structured anatomical regions, such as white matter in brain MRI or liver and lungs in CT, may require smoother deformation to counteract noise. In contrast, regions with more intricate structures may require more complex deformations for accurate registration.

Efforts have been made to develop regularizers that vary in space, including optimization-based registration schemes (e.g., Pace et al. (2013); Risser et al. (2013); Stefanescu et al. (2004); Vialard and Risser (2014); Gerig et al. (2014); Kabus et al. (2006)) and deep learning-based methods that learn spatially varying regularization from data (e.g., Niethammer et al. (2019); Shen et al. (2019)). In (Niethammer et al., 2019), Niethammer et al. proposed using DNNs to predict locally adaptive weights for multi-Gaussian kernels, but their method requires pre-setting the variance of the kernels and is not effective for end-to-end registration networks. Shen et al. (2019) expanded on the work of (Niethammer et al., 2019) by introducing an end-to-end training scheme to learn a spatially varying regularizer and the initial momentum in a spatiotemporal velocity setting. This method has the ability to track the deformation of regions and estimate a unique regularizer for each time point. However, the implementation of this method is not straightforward and cannot be seamlessly integrated with existing DNN-based methods.

In this paper, a novel DNN method is introduced for end-to-end learning of a spatially varying regularizer from data. The main contributions of this work are as follows:

- We propose a spatially varying regularization method for diffeomorphic image registration through unsupervised learning. At test time, it generates a subject-specific regularization map that controls regularization levels at the voxel level.

- The proposed method improves the registration performance of learning-based image registration, supports or approximates discontinuity-preserving registration, and provides an additional layer of interpretability for learning-based image registration.
- We integrate Bayesian optimization into the learning framework to enable automated tuning of optimal hyperparameters for any given image registration task.
- The proposed method is straightforward to implement. Although demonstrated using a specific DNN model, TransMorph, it can be seamlessly adapted to other DNN architectures without requiring major changes to the code.
- Comprehensive evaluations on publicly available datasets across various anatomical regions demonstrate that the proposed method improves the registration accuracy of the DNN backbone while preserving low deformation irregularities.
- To promote reproducible research, we provide the community with access to the source code and pre-trained models, which are publicly available at: <http://bit.ly/3BrXGxz>.

The remainder of the paper is organized as follows. Section 2 discusses related work. Section 3 describes the proposed methodology. The experimental setup, implementation details, and datasets used in this study are discussed in Sect. 4. Section 5 presents the experimental results. The findings drawn from these results are discussed in Sect. 6, and Sect. 7 concludes the paper.

## 2. Related Works

### 2.1. Diffusion Regularizer

In learning-based image registration, the diffusion regularizer is often used to impose deformation smoothness (Balakrishnan et al., 2019; Dalca et al., 2019b; Kim et al., 2021; Chen et al., 2022b, 2021a; Liu et al., 2022a). It is expressed as:

$$\mathcal{R}(\phi) = \sum_{\mathbf{p} \in \Omega} |\nabla \mathbf{u}(\mathbf{p})|^2, \quad (2)$$

where  $\mathbf{u}$  denotes the displacement field such that the deformation field  $\phi = \mathbf{id} + \mathbf{u}$ ,  $\mathbf{id}$  denotes the identity,  $\mathbf{p} = (p^x, p^y, p^z)$  is the voxel location, and  $\Omega \subset \mathbb{R}^3$  represents the 3D spatial domain. The operator,  $\nabla$ , computes the spatial gradients of each component of the displacement field. Specifically,  $\nabla \mathbf{u}(\mathbf{p}) = (\frac{\partial \mathbf{u}(\mathbf{p})}{\partial x}, \frac{\partial \mathbf{u}(\mathbf{p})}{\partial y}, \frac{\partial \mathbf{u}(\mathbf{p})}{\partial z})$ , which can be approximated through finite differences. For example, with the forward difference approximation, we have  $\frac{\partial \mathbf{u}(\mathbf{p})}{\partial x} \approx \mathbf{u}(p^x + 1, p^y, p^z) - \mathbf{u}(p^x, p^y, p^z)$ . As shown in Dalca et al. (2019a,b), this regularizer can be derived from the maximum a posteriori estimation of the variable  $\mathbf{u}$  assuming that the prior distribution on  $\mathbf{u}$  is a multivariate normal distribution with mean  $\boldsymbol{\mu} = \mathbf{0}$  and covariance  $\boldsymbol{\Sigma}$ , expressed as:  $p(\mathbf{u}) \propto \mathcal{N}(\mathbf{u}; \mathbf{0}, \boldsymbol{\Sigma})$ , where  $\boldsymbol{\Sigma}^{-1} = \boldsymbol{\Lambda}_{\mathbf{u}} = \lambda \mathbf{L}$ , and  $\mathbf{L} = \mathbf{D} - \mathbf{A}$  is the Laplacian of a neighborhood graph defined on the image grid. Here,  $\mathbf{D}$  is the degree matrix and  $\mathbf{A}$  is the adjacency matrix. The

parameter  $\lambda$  controls the smoothness of the displacement. The logarithm of this prior distribution can be simplified to Eqn. 2 as follows:

$$\begin{aligned} \log p(\mathbf{u}) &= \frac{1}{2} \log |\Sigma^{-1}| - \frac{1}{2} \mathbf{u}^\top \Sigma^{-1} \mathbf{u} + \text{const.} \\ &= \frac{1}{2} \log |\Lambda_{\mathbf{u}}| - \frac{1}{2} \mathbf{u}^\top \Lambda_{\mathbf{u}} \mathbf{u} + \text{const.} \\ &= -\frac{\lambda}{2} \mathbf{u}^\top \mathbf{L} \mathbf{u} + \text{const.} \\ &= -\frac{\lambda}{2} \sum_{\mathbf{p} \in \Omega} |\nabla \mathbf{u}(\mathbf{p})|^2 + \text{const.}, \end{aligned} \quad (3)$$

by noting the fact that  $\log |\Lambda_{\mathbf{u}}|$  is a constant, where  $|\Lambda_{\mathbf{u}}| = \det(\Lambda_{\mathbf{u}})$ . The parameter  $\lambda$  regulates the smoothness of the deformation by varying the covariance of the normal distribution. When  $\lambda$  increases, the covariance  $\Sigma$  decreases, resulting in greater similarity among neighboring displacements. This can also be understood as applying a larger variance Gaussian kernel to the displacement field, leading to a smoother deformation.

## 2.2. Probabilistic Inference of Regularization

Simpson et al. (2012) introduced a hierarchical probabilistic model that adaptively determines the level of regularization for each subject based on available data, rather than manually tuning the regularization hyperparameter for each subject. The model uses a free-form deformation approach, where the transformation is characterized by a set of control points,  $\boldsymbol{\omega}$ . The registration process is mathematically represented as  $\mathbf{f} = \mathbf{m} \circ \phi(\boldsymbol{\omega}) + \boldsymbol{\epsilon}$ . Here, the likelihood of the fixed image is described by a normal distribution, and prior distributions are placed on both the transformation parameters  $\boldsymbol{\omega}$  and the image noise  $\boldsymbol{\epsilon}$ . Specifically, the prior for  $\boldsymbol{\omega}$  is modeled using a multivariate normal distribution, as detailed in Sect. 2.1, while a gamma distribution is used for the prior modeling of  $\boldsymbol{\epsilon}$ . Additionally, a scalar spatial precision parameter  $\lambda$ , which arises from the multivariate normal distribution of  $\boldsymbol{\omega}$ , is modeled with a prior gamma distribution and serves to control the level of regularization. For inference, the method employs a mean-field variational Bayes approach, optimizing an objective function that comprises the log-likelihood and the negative Kullback-Leibler divergence between the approximate posterior distributions and the assigned priors. This results in a full probabilistic model that also captures the uncertainty associated with the transformation parameters.

This method proposed in Simpson et al. (2012) is optimization-based and, although it allows for the inference of different regularization parameters for each given image pair, the regularization remains spatially invariant across the image. In contrast, in this paper, we aim to infer varying levels of regularization strength at the voxel level using a deep learning framework. This enables us to implement spatially varying regularization and offers a significantly faster computational time compared to traditional optimization-based methods.

## 2.3. Learning Spatially Varying Regularizer

In Niethammer et al. (2019), a method for spatially varying regularization through metric learning was proposed. The

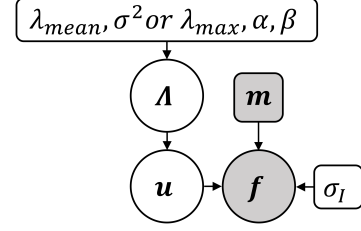


Fig. 1. The probabilistic dependencies of the model parameters are graphically illustrated in the diagram. Random variables are depicted as circles, while rounded squares represent model parameters. Shaded quantities indicate observed elements at test time, and the plate indicates replication given different samples.

approach involves learning locally adaptive weights for multiple Gaussian kernels with different standard deviations, in the form:  $\sum_{i=0}^{N-1} w_i(\mathbf{p}) G_i$ . Here,  $w_i(\mathbf{p})$  represents the weight of the  $i^{\text{th}}$  Gaussian kernel  $G$  at the voxel location  $\mathbf{p}$ , and they satisfy  $\sum_{i=0}^{N-1} w_i(\mathbf{p}) = 1$ . A neural network  $f$ , with parameters  $\theta$ , predicts these adaptive weights using input from the image pair and the initial momentum  $m_0$  generated by a traditional registration method. This can be represented as  $[w_0, \dots, w_{N-1}] = f_\theta(\mathbf{m}, \mathbf{f}, m_0)$ . Then, the deformation is smoothed by convolving the weighted multi-Gaussian kernel with  $m_0$ :

$$\sum_{i=0}^{N-1} \sqrt{w_i(\mathbf{p})} \int_{\mathbf{q}} G_i(\mathbf{p} - \mathbf{q}) \sqrt{w_i(\mathbf{q})} m_0(\mathbf{q}) d\mathbf{q}. \quad (4)$$

During network training, two loss functions were placed over  $w$ 's to promote smoothness in the momentum and adaptive weights. These loss functions included an optimal mass transport (OMT) loss and a total variational (TV) loss. The OMT loss forces the network to prioritize the use of the Gaussian kernel with the largest variance, while the TV loss encourages weight changes coinciding with image edges. Although successful in implementing spatially varying regularization, this method is not suitable for end-to-end registration networks because it requires initial momentum for network input. Additionally, the number and standard deviations of the Gaussian kernels, as well as the weighting parameters for OMT and TV losses, are hyperparameters that need extensive training cycles to optimize manually.

A parallel independent work (Wang et al., 2023) also explores spatially varying regularization, where varying regularization weights are allocated to different anatomical regions. Their approach presents a different mechanism that conditions a pre-defined weight map in the network architecture. To implement their approach, anatomical label maps of the input images are required, and the weights are directly imposed on the displacement gradients. Conversely, in our approach, we aim to determine the spatially varying regularization weight directly from the data without leaning on anatomical label maps, while adhering to a Bayesian framework that guarantees the mathematical integrity of the proposed method.

## 3. Methods

We define the moving and fixed images, respectively, as  $\mathbf{m}$  and  $\mathbf{f}$ . These images are defined over a 3D spatial domain, de-

noted as  $\mathbf{m}, \mathbf{f} \in \mathbb{R}^{H \times W \times D}$ . Here, we aim to develop a spatially varying deformation regularizer for end-to-end learning of deformable image registration, rather than a spatially invariant regularization for the entire deformation as used in almost all existing learning-based registration methods (e.g., Balakrishnan et al. (2019); Dalca et al. (2019b); Kim et al. (2021); Chen et al. (2022b); Mok and Chung (2021); Liu et al. (2022a); Chen et al. (2025)). In the proposed method, the image registration process is described through a probabilistic lens by using a hierarchical model. The details of this approach are expounded in the subsequent sections.

### 3.1. Hierarchical Model

Figure 1 depicts the graphical illustration of the proposed hierarchical model. Our objective is to compute the joint posterior probability of registration, denoted by  $p(\mathbf{u}, \mathbf{\Lambda} | \mathbf{f}; \mathbf{m})$ , through a maximum-a-posteriori (MAP) framework. Here,  $\mathbf{u}$  is a  $N_c \times 3$  matrix that symbolizes the displacement field, while  $\mathbf{\Lambda}$  is a  $N_c \times N_c$  matrix that functions as the spatial precision (i.e., the inverse covariance).  $N_c$  denotes the total number of voxels (i.e.,  $N_c = HWD$ ). We model  $\mathbf{\Lambda}$  as a *weighted* graph Laplacian matrix defined over the image grid. This matrix encodes spatial variations in the degree of regularization by assigning weights to the edges between adjacent voxels. Leveraging Bayes' theorem, we can express this joint posterior distribution as being directly proportional to the product of the hyperprior distribution of the spatial precision (i.e.,  $p(\mathbf{\Lambda})$ ), the population distribution of the displacement field given the spatial regularization (i.e.,  $p(\mathbf{u} | \mathbf{\Lambda})$ ), and the data likelihood (i.e.,  $p(\mathbf{f} | \mathbf{u}, \mathbf{\Lambda}; \mathbf{m})$ ). Mathematically, this relationship can be expressed as:

$$p(\mathbf{u}, \mathbf{\Lambda} | \mathbf{f}; \mathbf{m}) \propto p(\mathbf{\Lambda}) p(\mathbf{u} | \mathbf{\Lambda}) p(\mathbf{f} | \mathbf{u}, \mathbf{\Lambda}; \mathbf{m}). \quad (5)$$

We treat both  $\mathbf{u}$  and  $\mathbf{\Lambda}$  as unknown quantities to be estimated from the data. To this end, we jointly optimize the logarithm of the joint posterior over  $\mathbf{u}$  and  $\mathbf{\Lambda}$  using a Type-II MAP approach. This leads to:

$$\arg \max_{\mathbf{u}, \mathbf{\Lambda}} \log p(\mathbf{u}, \mathbf{\Lambda} | \mathbf{f}; \mathbf{m}) = \arg \max_{\mathbf{u}, \mathbf{\Lambda}} \log p(\mathbf{\Lambda}) + \log p(\mathbf{u} | \mathbf{\Lambda}) + \log p(\mathbf{f} | \mathbf{u}, \mathbf{\Lambda}; \mathbf{m}). \quad (6)$$

In this work, we model the data likelihood using the Boltzmann distribution:

$$p(\mathbf{f} | \mathbf{u}, \mathbf{\Lambda}; \mathbf{m}) \propto \exp(-\sigma_I \mathcal{D}_{NCC}(\mathbf{f}, \mathbf{m} \circ \phi_{\mathbf{u}})), \quad (7)$$

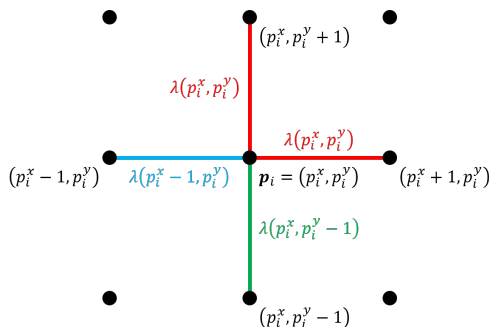


Fig. 2. Weighted graph Laplacian on a 2D image grid centered at  $\mathbf{p}_i$ . Red edges represent forward adjacency. Blue and green edges indicate backward adjacency. Each color corresponds to a distinct edge weight.

where  $\sigma_I$  is a user-defined hyperparameter (we set  $\sigma_I = 1$  throughout this study),  $\phi_{\mathbf{u}}$  denotes the deformation field that warps  $\mathbf{m}$  to  $\mathbf{f}$ , and  $\mathcal{D}_{NCC}(\cdot)$  denotes the negative normalized cross-correlation (NCC). The population and hyperprior distributions are described in the following sections.

### 3.2. Population Distribution

In accordance with Dalca et al. (2019b) and Simpson et al. (2012) and Sect. 2.1, we model the population distribution,  $p(\mathbf{u} | \mathbf{\Lambda})$ , by using a multivariate normal distribution:

$$\mathbf{u} | \mathbf{\Lambda} \sim \mathcal{N}(\mathbf{u}; \mathbf{0}, \mathbf{\Lambda}^{-1}) = \frac{|\mathbf{\Lambda}|^{\frac{3}{2}}}{(2\pi)^{\frac{3N_c}{2}}} \exp\left(-\frac{1}{2} \text{tr}(\mathbf{u}^T \mathbf{\Lambda} \mathbf{u})\right), \quad (8)$$

and

$$\mathbf{\Lambda} = \mathbf{D} - \mathbf{A}, \quad (9)$$

where  $\mathbf{D}$  and  $\mathbf{A}$  are the degree matrix and the adjacency matrix of a weighted graph Laplacian, respectively.

A representation of the weighted graph on a 2D image grid centered at  $\mathbf{p}_i$  is shown in Fig. 2. The dots show the voxel in the neighborhood of  $\mathbf{p}_i$ , and the edges show the adjacency and corresponding weights between  $\mathbf{p}_i$  and its neighbors. Specifically, the red edges show the forward adjacency, and the blue and green edges show the backward adjacency. The edge weights were designed such that edges with forward adjacency were assigned equal weights, e.g.,  $\lambda(p_i^x, p_i^y)$ , as highlighted in red in Fig. 2. Based on this design, the adjacency matrix  $\mathbf{A}$  is defined such that its element  $\mathbf{A}_{ij}$  is:

$$\mathbf{A}_{ij} = \begin{cases} \lambda(\mathbf{p}_i) & \text{if } \mathbf{p}_j \text{ is forward adjacent to } \mathbf{p}_i \\ 0 & \text{otherwise} \end{cases}, \quad (10)$$

where  $\mathbf{p}_i$  and  $\mathbf{p}_j$  correspond to voxel locations indexed by  $i$  and  $j$ , respectively, which from 1 to  $N_c$ . The forward adjacency in 3D denotes the condition that  $\mathbf{p}_j$  is adjacent to  $\mathbf{p}_i$  in the positive  $x$ ,  $y$ , or  $z$  direction (i.e.,  $\mathbf{p}_j \in \{(p_i^x + 1, p_i^y, p_i^z), (p_i^x, p_i^y + 1, p_i^z), (p_i^x, p_i^y, p_i^z + 1)\}$ ). This adjacency design arises from the computation of forward differences for the gradient operation in the diffusion regularizer (Eqn. 2). Note that the choice of edge weights and adjacency can be adapted for different finite-difference approximations. The diagonal degree matrix  $\mathbf{D}$  is similarly defined as:

$$\mathbf{D}_{ij} = \begin{cases} \sum_{k=1}^{N_c} \mathbf{A}_{ik} & \text{if } i = j \\ 0 & \text{otherwise} \end{cases}. \quad (11)$$

In these equations,  $\lambda(\mathbf{p})$  represents the regularization weight of the edges that are forward connected with the specific voxel location  $\mathbf{p}$ , which modulates the regularization strength at that location. With these considerations, we formulate the log-probability as follows:

$$\begin{aligned} \log p(\mathbf{u} | \mathbf{\Lambda}) &\propto 3 \log |\mathbf{\Lambda}| - \text{tr}(\mathbf{u}^T \mathbf{\Lambda} \mathbf{u}) \\ &= 3 \log |\mathbf{\Lambda}| - \sum_{\mathbf{p} \in \Omega} \lambda(\mathbf{p}) |\nabla \mathbf{u}(\mathbf{p})|^2. \end{aligned} \quad (12)$$

Since  $\mathbf{\Lambda}$  is related to the covariance of the multivariate normal distribution (as discussed in Sect. 2.1), employing a higher



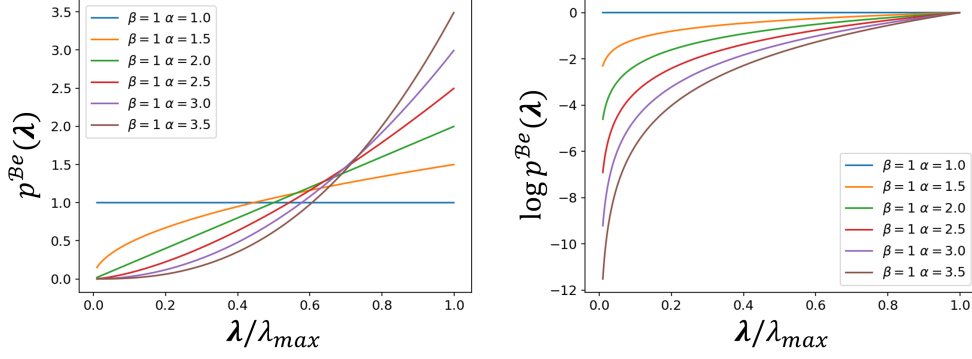


Fig. 3. The plots of  $p^{\text{Be}}(\lambda)$  and  $\log p^{\text{Be}}(\lambda)$  under the assumption of beta distribution, with varying shape parameter  $\alpha$ .

value for  $\lambda(\mathbf{p})$  virtually results in a stronger Gaussian smoothing at voxel location  $\mathbf{p}$ . The second term essentially constitutes a spatially varying version of the diffusion regularizer, which can be interpreted as the application of spatially-modulated multi-Gaussian kernels to the deformation — an approach resonating with the method proposed in Niethammer et al. (2019) (Sect. 2.3). This can be attributed to the fact that the convolution of multiple Gaussian kernels essentially results in a Gaussian kernel. However, we argue that the method proposed here is more apt for end-to-end training than the method in Niethammer et al. (2019), since we introduce a hyperprior distribution to  $\mathbf{\Lambda}$  and leverage the DNN to directly predict  $\lambda(\mathbf{p})$  — in other words, the Gaussian covariance — based on the given data. Thus, unlike the approach in Niethammer et al. (2019), the proposed method obviates the need to predetermine the number and variances of the Gaussians.

### 3.3. Hyperprior Distribution

The hyperprior distribution of spatial precision,  $\mathbf{\Lambda}$ , is probabilistically modeled via the scale family of distributions. The underlying intuition is that the strength of regularization across voxel locations adheres to a specific distribution, promoting regularization but permitting weaker regularization strength at certain voxel locations. It is important to note that the Laplacian matrix  $\mathbf{\Lambda}$  is intrinsically related to the spatial weights  $\lambda$ . Specifically,  $\mathbf{\Lambda}$  is a deterministic function of  $\lambda$ , constructed based on the edge weights represented by  $\lambda$  and the graph structure. As a result, modeling the distribution  $p(\lambda)$  effectively captures the hyperprior distribution  $p(\mathbf{\Lambda})$ .

In the context of this paper, the prior knowledge for  $\lambda$  emerges from the general preference to favor smooth deformations. That is, among all the potential solutions to the ill-posed problem of DIR, those that result in smooth deformations are particularly preferred. This preference suggests that  $\lambda(\mathbf{p})$  is more likely to have larger values to impose overall smoothness in the deformation field. Here, we consider two assumptions that  $\lambda$  is either normal- or beta-distributed, although alternative distribution types can also be considered depending on the application. Furthermore, ensuring spatial smoothness in  $\lambda$  is crucial to avert abrupt changes in regularization, which in turn could affect the smoothness of the deformation field. To impose smoothness in  $\lambda$ , we integrate a multivariate normal distribution in addition to

either the normal or beta distribution to model  $p(\lambda)$ . The resultant hyperprior distribution is expressed as the multiplication of two distributions: the first couples the elements of  $\lambda$  together, while the second characterizes the independent attributes of each element within  $\lambda$ :

$$p(\lambda) \propto \mathcal{N}(\lambda; \mathbf{0}, \Sigma_\lambda) p^{\text{NorBe}}(\lambda). \quad (13)$$

Analogous to Eqn. 3, the multivariate normal distribution simplifies to a diffusion regularizer placed over  $\lambda$ . Consequently, the log-hyperprior can be expressed as:

$$\log p(\lambda) \propto -\frac{\eta}{2} \sum_{\mathbf{p} \in \Omega} |\nabla \lambda(\mathbf{p})|^2 + \log p^{\text{NorBe}}(\lambda) + \text{const.} \quad (14)$$

In practice, this diffusion regularizer introduces a hyperparameter (i.e.,  $\eta$ ) that requires careful tuning. Rather than delving into this complexity, we employ a relaxed version of this regularizer: we estimate  $\lambda$  at a lower resolution and then upsampling it using bilinear interpolation. This effectively imparts the necessary smoothness to  $\lambda$  without additional complications. The modeling of  $p^{\text{NorBe}}(\lambda)$  is described in subsequent sections.

#### 3.3.1. Normal Distribution

We first opt for the scale family of normal distribution to model  $\lambda$ , owing to its simplicity and also motivated by the conjugate relationship that this normal prior holds with our earlier assumption of a multivariate normal distribution for the population distribution,  $p(\mathbf{u}|\lambda)$ . The definition is as follows:

$$\begin{aligned} p^{\text{N}}(\lambda) &\propto \mathcal{N}\left(\frac{\lambda}{\lambda_{\text{mean}}}; \mathbf{1}, \sigma^2\right) \\ &= \frac{1}{(\sqrt{2\pi}\sigma)^{N_c}} \exp\left(-\frac{1}{2\sigma^2} \left(\frac{\lambda}{\lambda_{\text{mean}}} - \mathbf{1}\right)^\top \left(\frac{\lambda}{\lambda_{\text{mean}}} - \mathbf{1}\right)\right), \end{aligned} \quad (15)$$

and

$$\begin{aligned} \log p^{\text{N}}(\lambda) &\propto -\frac{1}{2\sigma^2} \left(\frac{\lambda}{\lambda_{\text{mean}}} - \mathbf{1}\right)^\top \left(\frac{\lambda}{\lambda_{\text{mean}}} - \mathbf{1}\right) + \text{const.} \\ &= -\frac{1}{2\sigma^2} \sum_{\mathbf{p} \in \Omega} \left(\frac{\lambda(\mathbf{p})}{\lambda_{\text{mean}}} - 1\right)^2 + \text{const.}, \end{aligned} \quad (16)$$

where  $\sigma$  is the standard deviation and  $\lambda_{\text{mean}}$  acts as a scale parameter that determines the overall regularization strength. Notably,

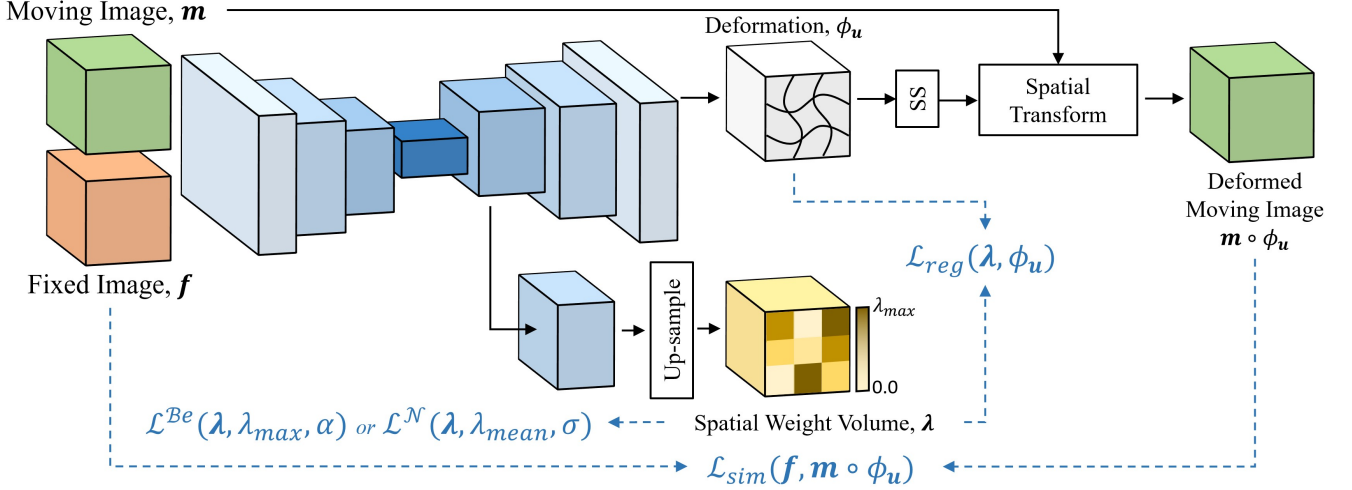


Fig. 4. The overall framework of the proposed method for unsupervised learning of spatially varying regularization for diffeomorphic image registration. The method introduces lightweight ConvNet blocks that take the feature maps from the bottleneck layers of the registration network to generate a spatial weight volume  $\lambda$ , assigning regularization at the voxel level. The spatial weight volume is used to regularize the deformation during training. Additionally, the spatial weight volume is itself regularized by an auxiliary term (i.e.,  $\mathcal{L}^{N\text{or}Be}(\lambda)$ ), promoting smoother deformations when appropriate. While the framework is demonstrated using TransMorph as the registration backbone, it is agnostic to the choice of registration networks and can be easily adapted to other architectures.

a larger  $\lambda_{mean}$  virtually inflates the mean of the normal distribution, yielding larger values of  $\lambda(\mathbf{p})$  and, therefore, stronger regularization, and vice versa. As outlined in Eqn. 12,  $\lambda$  is associated with covariance, hence it cannot have values less than 0. In practice, this results in a one-sided truncated normal distribution for the prior. However, the absence of a specific upper limit can cause excessive regularization, particularly at the tail end of the distribution, complicating the selection of optimal values for  $\lambda_{mean}$  and  $\sigma$ . In the hyperparameter optimization process, we optimize  $\sigma' = \frac{1}{2\sigma^2}$  directly, rather than  $\sigma$ , to simplify the tuning process.

In the following section, we propose using the beta distribution to model the hyperprior distribution of  $\lambda$ , which presents a more controlled approach to regularization by defining the upper and lower bounds for the values  $\lambda$  can take.

### 3.3.2. Beta Distribution

Our choice of the beta distribution for the hyperprior arises from its ability to facilitate an upper bound for regularization strength, while also providing the flexibility to give a higher likelihood to the user-defined upper bound. Therefore, we adopt the scale family of beta distribution for  $\lambda$ , which can be mathematically expressed as:

$$p^{Be}(\lambda) \propto \prod_{\mathbf{p} \in \Omega} \text{Be}\left(\frac{\lambda(\mathbf{p})}{\lambda_{max}}; \alpha, \beta\right) \\ = \prod_{\mathbf{p} \in \Omega} \frac{\Gamma(\alpha + \beta)}{\Gamma(\alpha)\Gamma(\beta)} \left(\frac{\lambda(\mathbf{p})}{\lambda_{max}}\right)^{\alpha-1} \left(1 - \frac{\lambda(\mathbf{p})}{\lambda_{max}}\right)^{\beta-1}, \quad (17)$$

and

$$\log p^{Be}(\lambda) \\ \propto \sum_{\mathbf{p} \in \Omega} \left( (\alpha - 1) \log \frac{\lambda(\mathbf{p})}{\lambda_{max}} + (\beta - 1) \log \left(1 - \frac{\lambda(\mathbf{p})}{\lambda_{max}}\right) \right) + \text{const.} \\ = (\alpha - 1) \sum_{\mathbf{p} \in \Omega} \log \frac{\lambda(\mathbf{p})}{\lambda_{max}} + \text{const.}, \quad (18)$$

where  $\lambda(\mathbf{p}) \in [0, \lambda_{max}]$ ,  $\lambda_{max} > 0$  is a hyperparameter that controls the maximum regularization strength by scaling the distribution,  $\Gamma(\cdot)$  denotes the Gamma function, and  $\alpha$  and  $\beta$  are shape parameters that define the shape of the beta distribution. We set  $\beta = 1$  and choose an  $\alpha$  value greater than or equal to 1 (i.e.,  $\alpha \geq 1$ ), encouraging a higher regularization strength (i.e., a larger value of lambda) to be more probable. This specific instance of the beta distribution is also known as a power-function distribution. As shown in Fig. 3, altering  $\alpha$  effectively allows us to modulate the penalty applied to  $\lambda(\mathbf{p})$ . Specifically, an  $\alpha$  value of 1 yields a uniform distribution, inflicting no penalty, thus allowing  $\lambda(\mathbf{p})$  to assume any value within its range. A larger  $\alpha$ , however, pushes  $\lambda(\mathbf{p})$  towards  $\lambda_{max}$ . Unlike a normal distribution model for  $p(\lambda)$ , the beta distribution extends the advantage of bounding the regularization strength within a specified range, with a minimum of 0, implying no regularization, and a maximum set by  $\lambda_{max}$ . In practice, rather than tuning  $\alpha$ , we optimize  $\alpha' = \alpha - 1$  to simplify hyperparameter optimization.

### 3.4. Loss Function

In this subsection, we elaborate on how the loss function is formulated, following from Eqn. 6. The aim is to maximize the log joint posterior, which is equivalent to minimizing its

negative. Therefore, the loss function can be expressed as:

$$\mathcal{L}(\mathbf{m}, \mathbf{f}, \mathbf{u}, \boldsymbol{\lambda}) = \mathcal{D}_{NCC}(\mathbf{f}, \mathbf{m} \circ \phi_{\mathbf{u}}) + \sum_{\mathbf{p} \in \Omega} \lambda(\mathbf{p}) |\nabla \mathbf{u}(\mathbf{p})|^2 - \mathcal{L}^{\text{NorBe}}(\boldsymbol{\lambda}). \quad (19)$$

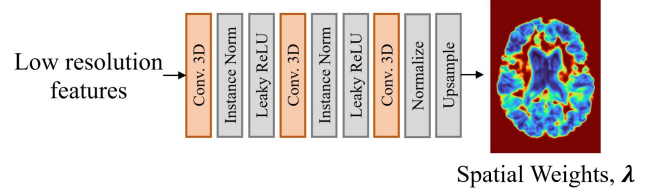


Fig. 5. The schematic of the ConvNet block that produces the spatial weight volume,  $\lambda$ .

For the last term,  $\mathcal{L}^{\text{NorBe}}(\boldsymbol{\lambda})$ , we specify it based on either Eqn. 16 or Eqn. 18, depending on whether a normal or beta distribution model is employed, i.e.,  $\mathcal{L}^{\text{NorBe}}(\boldsymbol{\lambda}) = \log p^{\text{NorBe}}(\boldsymbol{\lambda})$ . Note that the term  $\log |\mathbf{A}|$  from Eqn. 12 is excluded from the loss function and this exclusion is justified by three main factors. Firstly, the computation of  $\log |\mathbf{A}|$  is non-trivial, computationally intensive, and prone to numerical instability due to the determinant computation of a large sparse matrix with dimensions  $N_c \times N_c$ . Secondly, this term mainly aims to enhance spatial precision (or reduce covariance) in the multivariate normal distribution that governs  $\mathbf{u}$ . However, an informative hyperprior distribution is already imposed on  $\mathbf{A}$  to control this spatial precision, rendering the inclusion of  $\log |\mathbf{A}|$  less crucial. Lastly, the prior elements in  $|\mathbf{A}|$  are not independent, but are coupled together. As elaborated in Sect. 3.3, this coupling is modeled via a multivariate normal distribution facilitated by the upsampling operation. Hence, by omitting the higher-order term in  $\log |\mathbf{A}|$  in favor of  $\log p^{\text{NorBe}}(\boldsymbol{\lambda})$ , which characterizes the individual elements in  $\mathbf{A}$ , we attain a more concise representation of the prior.

It is also important to note the intrinsic connection between  $\mathcal{L}^{\text{Be}}(\boldsymbol{\lambda})$  and binary entropy loss. As  $\frac{\lambda(\mathbf{p})}{\lambda_{\max}} \in [0, 1]$  can be viewed as a "probability" map produced by the network, with a target probability map of 1 and the weight of the loss controlled by  $1 - \alpha$ .

### 3.5. Registration Neural Network

Fig. 4 shows the overall framework of the proposed method. We used a neural network to take in moving and fixed images,  $\mathbf{m}$  and  $\mathbf{f}$ . The network outputs a deformation field  $\phi_{\mathbf{u}} \in \mathbb{R}^{3 \times H \times W \times D}$  that warps  $\mathbf{m}$  to  $\mathbf{f}$ , as well as a spatial weight volume  $\boldsymbol{\lambda} \in \mathbb{R}^{H \times W \times D}$ . We then used this weight volume to apply spatially varying regularization strength to different voxels through a *weighted diffusion regularizer* (i.e., the second term in Eqn. 19). The backbone registration network we employed builds upon our previously proposed TransMorph (Chen et al., 2022a,b), which has shown effective results in multiple registration applications. It is important to note that the proposed spatially varying regularization framework is not restricted to this architecture and can be seamlessly extended to other network designs. The TransMorph network employs a Swin Transformer encoder (Liu et al., 2021) and a ConvNet decoder, which generates a set of deformation fields. These fields are then composed to form the final deformation field. As shown in Fig. 4, an additional convolution block comprising three convolutional layers is introduced within the decoder of the TransMorph and applied to the 1/4 resolution branch, resulting in the generation of the weight volume  $\boldsymbol{\lambda}$ . The final weight volume is subsequently up-sampled using bilinear interpolation to align with the resolution of the deformation field. As mentioned in Sect. 3.3, by generating the weight volume at a lower resolution, we were able to reduce computational workload and introduce spatial

smoothness in the weight volume, which aligns with the physical interpretation of these weights.

### 3.6. Diffeomorphic Image Registration

As the proposed network learns to impose spatially varying regularization, certain regions may experience weak or even absent regularization, which could result in less realistic deformations. To address this, we enforce diffeomorphic image registration by interpreting the displacement field  $\mathbf{u}$ , estimated by the neural network, as an approximation of a stationary velocity field  $\mathbf{v}$ . We implement a time-stationary setting by exponentiating this velocity field using the *scaling-and-squaring* (SS) approach (Arsigny et al., 2006; Ashburner, 2007), mathematically expressed as:

$$\phi = \exp(\mathbf{v}) = \left( \exp(2^{-N} \mathbf{v}) \right)^{2^N}, \quad (20)$$

where  $\mathbf{v}$  is derived from  $\mathbf{u}$  and used to accumulate transformations in a smooth and invertible way. We opt for the SS approach for its straightforward implementation. However, the proposed method can also accommodate a time-varying setting if desired.

For the remainder of this paper, the proposed method is denoted as TM-SPR to emphasize the use of the spatially varying regularizer (SPR).

### 3.7. Automatic Hyperparameter Tuning

The proposed method requires tuning two hyperparameters:  $\lambda_{\text{mean}}$  and  $\sigma'$  when using a Gaussian prior, or  $\lambda_{\text{max}}$  and  $\alpha'$  when using a beta prior. Instead of employing computationally expensive grid search, we employed Bayesian optimization (BO) through the Tree-Structured Parzen Estimator (TPE) for hyperparameter optimization (Bergstra et al., 2011; Watanabe, 2023). BO optimizes the objective function (specifically the Dice score in our case) on the validation dataset by building a probabilistic model and using it to determine the next set of hyperparameters to sample. This approach is more efficient than grid search because it selectively explores the hyperparameter space, focusing on regions that are more likely to yield improvements. Furthermore, BO incorporates pruning, which enables early stopping of unpromising trials, further enhancing sample efficiency (Watanabe, 2023; Ozaki et al., 2020). For this study, we implemented BO using the open source Optuna package (Akiba et al., 2019), which fully automates hyperparameter tuning and analysis.



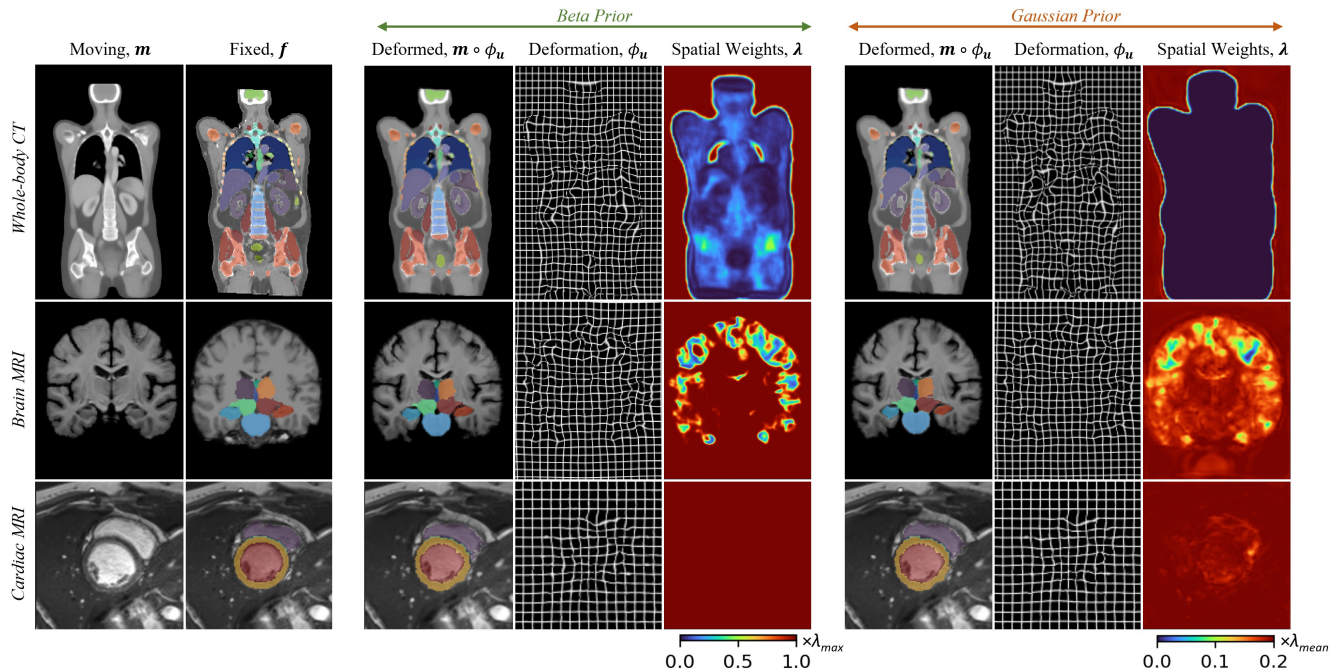


Fig. 6. Qualitative results of the proposed method across three registration tasks: atlas-to-subject whole-body CT registration (autoPET), inter-subject brain MRI registration (IXI), and intra-subject cardiac MRI registration (ACDC M&Ms) from top to bottom. The left panel displays the moving image and fixed image, with selected label maps overlaid on the fixed image. The middle panel illustrates the deformed moving image, deformation field, and spatial weight volume generated by the proposed method using the beta prior with optimal hyperparameters identified through BO. The right panel presents the corresponding results obtained using the Gaussian prior with optimal hyperparameters identified through BO.

## 4. Experiments

### 4.1. Dataset and Pre-processing

The proposed registration method was extensively evaluated using three publicly available data sets that cover a broad spectrum of anatomical regions and imaging applications. The descriptions of each dataset, along with the associated pre-processing steps, are provided in the subsequent paragraphs.

**IXI.** The IXI dataset<sup>1</sup> comprises 576 T1-weighted brain MRI images, with a distribution of 403 volumes for training, 58 volumes for validation, and 115 volumes for testing. Furthermore, a moving image, which was a brain atlas image obtained from Kim et al. (2021), was used for the atlas-to-patient registration task. All images went through a standard preprocessing pipeline through FreeSurfer (Fischl, 2012). This involved resampling to a uniform voxel size of  $1 \times 1 \times 1$  mm, affine registration, skull-stripping, and intensity normalization. After preprocessing, the image volumes were consistently cropped to a size of  $160 \times 192 \times 224$ . Anatomical label maps that include more than 30 anatomical structures were produced using FreeSurfer to evaluate registration performances. The registration task associated with this dataset is atlas-to-patient registration.

**ACDC and M&Ms.** The ACDC dataset (Bernard et al., 2018) includes 150 subjects, while the M&Ms dataset (Campello et al., 2021) comprises 320 subjects, making a total of 470

subjects. Each subject is represented by two frames corresponding to the end-diastolic (ED) and end-systolic (ES) phases. The datasets provide manual delineations of the left ventricle (LV) and right ventricle (RV) blood pools, as well as the left ventricular myocardium (MYO). Data were split into training, validation, and testing sets with 259, 61, and 150 subjects, respectively. All images were resampled to a uniform spatial resolution of  $1.5 \times 1.5 \times 3.5$  mm and adjusted to a volume of interest (VOI) of  $128 \times 128 \times 32$ , centered around the heart. Furthermore, the intensity values of the images were normalized using a min-max normalization to scale between 0 and 1. The primary registration challenge in this dataset involves intra-subject registration between the ED and ES stages.

**autoPET.** The autoPET dataset (Gatidis et al., 2022) comprises whole-body PET/CT scans from 900 cancer patients. However, only CT data were used in this study. Of the total, 628 were allocated for training, 90 for validation, and 178 for testing purposes. The segmentation of 104 classes in CT images was facilitated by the TotalSegmentor (Wasserthal et al., 2022). Our study focused on 103 of these classes, excluding the face. Resampling was first applied to all images, setting the voxel size to  $2.8 \times 2.8 \times 3.8$  mm. Subsequently, the images were affinely aligned with a common reference, chosen randomly from the patient pool, using the ANTs package (Avants et al., 2009). The post-alignment images were then cropped to dimensions  $192 \times 192 \times 256$ . Intensity values were truncated to fall within the  $[-300, 300]$  range and subsequently normalized to  $[0, 1]$ , enhancing the contrast for soft tissues. A CT atlas and associated anatomical label maps were constructed in Chen et al. (2023a) using an atlas construction

<sup>1</sup><https://brain-development.org/ixi-dataset/>



**Table 1. Search range of hyperparameters used in the Bayesian hyperparameter optimization.**

Dataset	$\lambda_{mean}$	$\sigma'$	$\lambda_{max}$	$\alpha'$
Whole-body CT ( <i>autoPET</i> )	[0.8, 3]	[0, 2]	[0.8, 3]	[0.0, 0.1]
Brain MRI ( <i>IXI</i> )	[0.5, 5]	[0, 4]	[0.5, 5]	[0.0, 0.2]
Cardiac MRI ( <i>ACDC M&amp;Ms</i> )	[0.8, 3]	[0, 2]	[0.8, 3]	[0.0, 0.6]

method described in (Dalca et al., 2019a). The registration task associated with this dataset is atlas-to-subject registration.

#### 4.2. Baseline Methods

To comprehensively evaluate the benefits of the proposed spatially varying regularization, we compared it with several well-established baseline methods. These included two traditional optimization-based approaches: SyN from the ANTs package (Avants et al., 2008), widely considered the state-of-the-art for neuroimaging, and deedsBCV (Heinrich et al., 2013), a leading method for abdominal registration.

We also assessed our method against VoxelMorph (Balakrishnan et al., 2019), a classical unsupervised ConvNet-based method, enhanced with augmented parameter scaling as suggested in (Jian et al., 2024) for improved performance. Additionally, we conducted comparisons with TransMorph (Chen et al., 2022b), the backbone network used in the proposed method, to assess the impact of introducing spatially varying regularization. For both VoxelMorph and TransMorph, we employed commonly used hyperparameter settings during training (Balakrishnan et al., 2019; Meng et al., 2024), setting the weights for the image similarity measure (NCC) and the deformation regularization (diffusion regularizer) equally to 1.

Furthermore, we evaluated the proposed approach against HyperMorph (Hoopes et al., 2022), a hyperparameter optimization framework that selects regularization parameters based on a validation dataset. For a fair comparison, we extended HyperMorph to TransMorph by integrating its hyperparameter learning framework while maintaining the same backbone network as the proposed method, denoted as Hyper-TransMorph. This ensures that performance differences can be attributed specifically to spatially varying regularization.

For all deep learning-based models, we consistently used NCC as the image similarity measure and the diffusion regularizer for deformation regularization. The detailed implementation of each method is provided below.

- SyN (Avants et al., 2008): A diffeomorphic image registration method from the ANTs package. We employed the "antsRegistrationSyN.sh" pipeline optimized for atlas-based registration with the "SyNOnly" option and cross-correlation as the similarity measure.
- deedsBCV (Heinrich et al., 2013): An optimization-based method using discrete optimization strategies with MIND-SSC (Heinrich et al., 2012) as the similarity measure. For the whole-body CT registration task, the grid spacing, search radius, and quantization step were set to [8, 7, 6, 5, 4], [8, 7, 6, 5, 4], and [5, 4, 3, 2, 1], respectively,

based on default settings optimized for abdominal registration. For brain MRI registration, we followed recommendations in (Hoffmann et al., 2021) for neuroimaging, setting the grid spacing, search radius, and quantization step to [6, 5, 4, 3, 2], [6, 5, 4, 3, 2], and [5, 4, 3, 2, 1], respectively. For cardiac MRI registration, we used the same hyperparameters as brain MRI registration, considering the smaller anatomical variability in intra-patient images.

- VoxelMorph (Balakrishnan et al., 2019): An unsupervised learning-based model with a U-Net backbone (Ronneberger et al., 2015). We adopted an enhanced version with an expanded model size, as proposed in (Jian et al., 2024), setting the encoder and decoder filters to [16, 32, 64, 96, 128] and [128, 96, 64, 32], respectively.
- HyperMorph (Hoopes et al., 2021): A framework for learning regularization hyperparameters using an auxiliary network. The auxiliary network comprises multiple small sub-networks, each consisting of five fully connected layers with [32, 64, 64, 128, 128] units, activated by ReLU, followed by a linearly activated fully connected layer to predict the parameters for a specific trainable layer in the registration network. The number of these sub-networks matches the number of trainable layers in the registration network. In this study, HyperMorph was applied to VoxelMorph, as described in the original work. The regularization hyperparameter  $\lambda$  was provided as input to the auxiliary network, while the weight for the image similarity term in the loss function was set to  $1 - \lambda$  during training, as was done similarly in Hoopes et al. (2021).
- TransMorph (Chen et al., 2022b): A Transformer-based registration model. We employed an improved version (Chen et al., 2022a), which demonstrated superior performance compared to the original model and served as our baseline.
- Hyper-TransMorph: An extension of TransMorph integrating the HyperMorph framework to enable hyperparameter learning while retaining the Transformer-based backbone.

#### 4.3. Implementation Details

The models were trained for 500 epochs using the Adam optimizer (Kingma and Ba, 2014) with a batch size of 1 and a learning rate of 0.0001. The TM-TVF (Chen et al., 2022a) model was configured with 7 time steps, and the number of integration steps for SS (i.e.,  $N$  in Eqn. 20) to enforce diffeomorphic registration was also set to 7. The implementation was carried out using the PyTorch framework, and training was performed on NVIDIA GPUs, including the RTX 3090, RTX Titan, RTX A6000, and H100.

For hyperparameter tuning, we conducted 50 trials for each experiment using Optuna. The specific search ranges for the hyperparameters,  $\lambda_{mean}$  and  $\sigma^2$  for the Gaussian prior, or  $\lambda_{max}$  and  $\alpha$  for the beta prior, are detailed in Table 1. Additionally, we applied a median pruner with a startup trial of 5, a warm-up step of 30, and an interval step of 10 to optimize the search process throughout the study.

**Table 2. Quantitative results for atlas-to-subject whole-body CT registration on the autoPET dataset. Top-performing results are highlighted in bold, and second-best results are indicated in *italic*. Statistically significant improvements, measured using the Wilcoxon signed-rank test, of the TransMorph variant over the backbone TransMorph are denoted by \*\* (\*\*: p-value < 0.001; \*: p-value < 0.01).**

Whole-body CT Registration (autoPET)			
Method	Dice $\uparrow$	% $ J  \leq 0$ $\downarrow$	%NDV $\downarrow$
Initial	0.403 $\pm$ 0.252	-	-
SyN	0.633 $\pm$ 0.263	0.00%	0.00%
deedsBCV	0.631 $\pm$ 0.254	0.00%	0.00%
VoxelMorph	0.622 $\pm$ 0.273	0.03%	0.00%
HyperMorph	0.638 $\pm$ 0.277	0.07%	0.38%
TransMorph	0.661 $\pm$ 0.267	0.00%	0.00%
Hyper-TransMorph	0.674 $\pm$ 0.267**	0.00%	0.00%
TM-SPR <sub>Gaussian</sub>	0.670 $\pm$ 0.272**	0.00%	0.00%
TM-SPR <sub>Beta</sub>	<b>0.677<math>\pm</math>0.268**</b>	0.00%	0.00%

#### 4.4. Evaluation Metrics

To evaluate the registration performance, we measured the overlap of anatomical label maps between the fixed image and the deformed moving image using the Dice coefficient. Given the focus on unsupervised image registration in this study, label maps were not used during the training phase. Thus, the Dice score serves as an indirect but adequate metric to assess registration accuracy. To assess the smoothness of the deformation fields, we used the percentage of non-positive Jacobian determinants ( $\%|J| \leq 0$ ) and the non-diffeomorphic volume ( $\%NDV$ ), as described in (Liu et al., 2024a). These metrics provide more accurate evaluations of the invertibility of the deformation under the finite-difference approximation.

## 5. Results

### 5.1. Whole-body Image Registration Results on the autoPET Dataset

1) *Qualitative Evaluation.* The top row of Fig. 6 presents the qualitative results of the proposed spatially varying regularization with optimized hyperparameters derived under two priors: beta (middle panel) and Gaussian (right panel). The spatial weight volume,  $\lambda$ , learned under both priors consistently favors smaller regularization weights within the body region. The Gaussian prior represents an extreme case, applying near-zero regularization within the body, whereas the beta prior assigns stronger regularization weights to central regions of organs where intensity differences between the moving and fixed images are smaller, such as in the lungs and pelvis. This behavior highlights the beta prior’s potential to adaptively modulate regularization based on local image characteristics in whole-body image registration.

The regions of low regularization observed with both priors underscore the importance of the proposed approach in enforcing diffeomorphic registration within a time-stationary framework. Without such a strategy, deformations within the body are likely to become irregular and unrealistic, which is highly undesirable for medical image registration (Chen et al., 2025). Additional qualitative comparisons between different registration methods are shown in Fig. A.14 in the appendix.

2) *Quantitative Evaluation.* Table 2 presents quantitative comparisons between different registration methods. The results indicate that learning-based models outperform optimization-based methods for this task, with SyN and deedsBCV achieving mean Dice scores of 0.633 and 0.631, respectively. Among learning-based models, TransMorph-based approaches outperform ConvNet-based models, i.e., VoxelMorph and HyperMorph, which optimizes the regularization hyperparameter  $\lambda$  (as defined in Eqn. 3). Specifically, VoxelMorph achieves a mean Dice score of 0.621, and HyperMorph improves this to 0.638. In comparison, TransMorph, which uses a fixed  $\lambda$  value of 1 without optimization, achieves a higher mean Dice score of 0.661.

The three TransMorph-based models capable of selecting optimal hyperparameters (i.e., Hyper-TransMorph, TM-SPR<sub>Gaussian</sub>, and TM-SPR<sub>Beta</sub>) demonstrate statistically significant improvements over TransMorph with a fixed regularization parameter ( $\lambda$  in Eqn. 3 set to 1) and no hyperparameter optimization. Among these models, TM-SPR<sub>Beta</sub> achieves the highest mean Dice score of 0.677, followed by Hyper-TransMorph at 0.674, and TM-SPR<sub>Gaussian</sub> at 0.670. Although the performance of TM-SPR<sub>Beta</sub> and Hyper-TransMorph is very similar, a statistically significant difference is observed between the two under the Wilcoxon signed-rank test ( $p = 0.009$ ).

These results highlight the prominence of the proposed spatially varying regularization for whole-body CT registration. The comparable mean Dice scores of Hyper-TransMorph and TM-SPR models can be attributed to the nature of the task, which favors minimal regularization (i.e.,  $\lambda$  approaches 0). For instance, the optimal hyperparameter for Hyper-TransMorph is 0.06, while for the spatially varying regularization models under the beta and Gaussian priors, the parameters enforcing larger values in the spatial weight volume  $\lambda$  (i.e.,  $\alpha'$  and  $\sigma'$ ) are also close to zero, at 0.027 and 0.005, respectively, as shown in Table 5. Consequently, the spatial weights within the body regions remain quite small and near zero, as illustrated in Fig. 7. Theoretically, when deformation regularization is minimal or absent, Hyper-TransMorph, TM-SPR<sub>Beta</sub>, and TM-SPR<sub>Gaussian</sub> effectively converge to the baseline TransMorph model with no deformation regularization (i.e.,  $\lambda = 0$ ). This convergence explains the similar performance observed among these models.

A detailed comparison of Dice scores across various methods for different anatomical structures in whole-body CT is illustrated using box plots in Fig. A.15 in the appendix.

In terms of regularity of deformation, optimization-based methods produced highly regularized deformations. Among learning-based methods, VoxelMorph and HyperMorph exhibited greater deformation irregularities due to the absence of diffeomorphism constraints. In contrast, TransMorph-based methods produced highly regularized deformations, benefiting from the imposed diffeomorphic registration achieved through the time-stationary velocity framework.

### 5.2. Brain Image Registration Results on the IXI Dataset

1) *Qualitative Evaluation.* The middle row of Fig. 6 shows the qualitative results of the proposed spatially varying regularization applied to brain MRI registration, with results derived

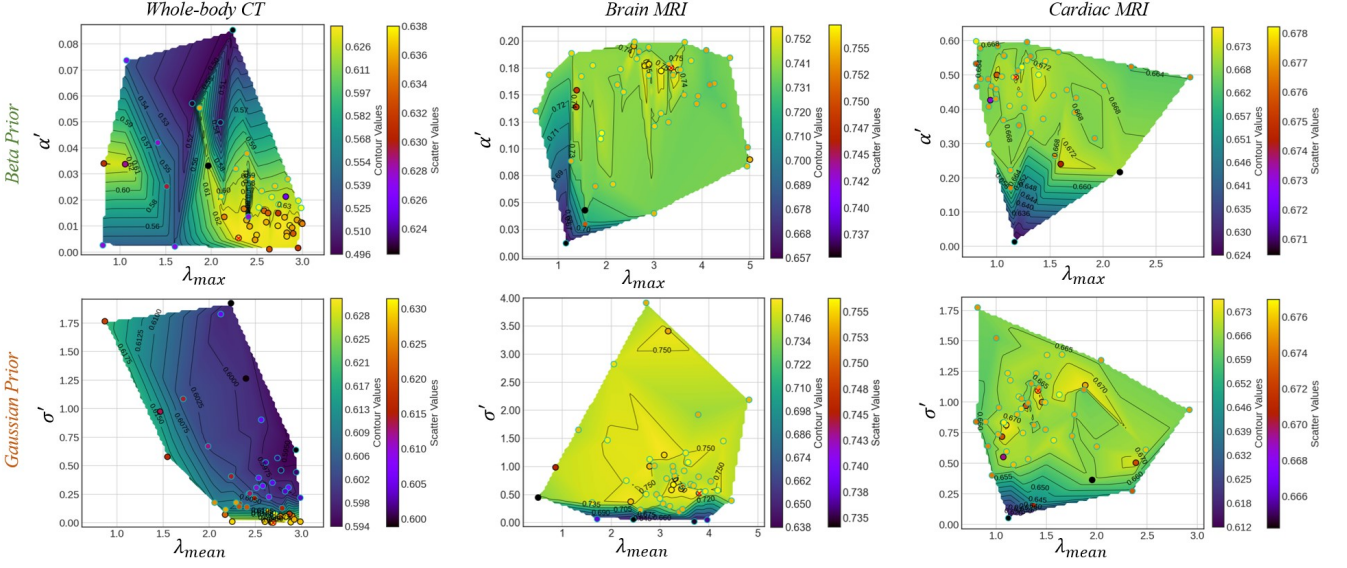


Fig. 7. Hyperparameter surface maps obtained through Bayesian Optimization (BO) for  $\alpha'$  and  $\lambda_{max}$  (beta prior) and  $\sigma'$  and  $\lambda_{mean}$  (Gaussian prior), evaluated on the validation set across three registration tasks: whole-body CT registration (*autoPET*), brain MRI registration (*IXI*), and cardiac MRI registration (*ACDC M&Ms*) from left to right. Scatter points with black edges represent trials that completed the full training cycle, while those with cyan edges indicate trials pruned before completion.

Table 3. Quantitative results for atlas-to-subject brain MRI registration on the IXI dataset. Top-performing results are highlighted in bold, and second-best results are indicated in *italic*. Statistically significant improvements, measured using the Wilcoxon signed-rank test, of the TransMorph variant over the backbone TransMorph are denoted by \*\* (\*\*: p-value < 0.001; \*: p-value < 0.01).

Brain MRI Registration (IXI)			
Method	Dice $\uparrow$	% $ J  \leq 0 \downarrow$	%NDV $\downarrow$
Initial	0.386 $\pm$ 0.195	-	-
SyN	0.758 $\pm$ 0.126	0.00%	0.00%
deedsBCV	0.740 $\pm$ 0.127	0.05%	0.02%
VoxelMorph	0.744 $\pm$ 0.131	4.33%	1.74%
HyperMorph	0.753 $\pm$ 0.131	0.38%	0.08%
TransMorph	0.757 $\pm$ 0.126	0.00%	0.00%
Hyper-TransMorph	0.762 $\pm$ 0.127**	0.00%	0.00%
TM-SPR <sub>Gaussian</sub>	<b>0.767<math>\pm</math>0.127**</b>	0.00%	0.00%
TM-SPR <sub>Beta</sub>	0.767 $\pm$ 0.129**	0.00%	0.00%

Table 4. Quantitative results for intra-subject cardiac MRI registration on the ACDC and the M&Ms datasets. Top-performing results are highlighted in bold, and second-best results are indicated in *italic*. Statistically significant improvements, measured using the Wilcoxon signed-rank test, of the TransMorph variant over the backbone TransMorph are denoted by \*\* (\*\*: p-value < 0.001; \*: p-value < 0.01).

Cardiac MRI Registration (ACDC M&Ms)			
Method	Dice $\uparrow$	% $ J  \leq 0 \downarrow$	%NDV $\downarrow$
Initial	0.537 $\pm$ 0.166	-	-
SyN	0.678 $\pm$ 0.138	0.00%	0.00%
deedsBCV	<b>0.740<math>\pm</math>0.121</b>	0.00%	0.00%
VoxelMorph	0.689 $\pm$ 0.128	0.44%	0.17%
HyperMorph	0.647 $\pm$ 0.141	0.08%	0.20%
TransMorph	0.711 $\pm$ 0.126	0.00%	0.00%
Hyper-TransMorph	0.698 $\pm$ 0.127	0.00%	0.00%
TM-SPR <sub>Gaussian</sub>	0.733 $\pm$ 0.120**	0.00%	0.00%
TM-SPR <sub>Beta</sub>	0.735 $\pm$ 0.119**	0.00%	0.00%

from the beta prior in the middle panel and the Gaussian prior in the right panel. For both priors, the learned spatial weight volume (i.e.,  $\lambda$ ) is observed to yield smaller values toward the cortical regions of the brain, where greater shape variability exists across images and patients, resulting in weaker deformation regularization. In contrast, the values in the  $\lambda$  increase in the deeper subcortical regions, indicating a stronger deformation regularization in these areas.

These patterns are more pronounced under the beta prior, which provides a  $\lambda$  that is more structured and interpretable. In contrast, while the Gaussian prior demonstrates a similar trend, its  $\lambda$  appears to be more complex and less coherent compared to those derived from the beta prior. Importantly, the regions with near-zero values in  $\lambda$  are consistent across both priors, predominantly located near the cortical regions.

Despite weaker regularization in certain areas, the deformation fields remain overall smooth, as shown in Fig. 6. This smoothness can be attributed to two key factors. First, the overall regularization strength per voxel is relatively high, as indicated by the values  $\lambda_{max} = 3.354$  and  $\lambda_{mean} = 3.796$  in Table 5. Although some regions exhibit smaller spatial weights, the combination of larger  $\lambda_{max}$  and  $\lambda_{mean}$  with the spatial weight volume,  $\lambda$ , collectively enforces strong regularization across voxels, resulting in an overall smooth deformation field. Second, the time-stationary framework effectively enforces diffeomorphic registration, which further contributes to the observed smoothness.

Additional qualitative comparisons of different registration methods on the brain MRI registration task are shown in Fig. B.16 in the appendix.



**Table 5. Optimal regularization hyperparameters identified through grid search for Hyper-TransMorph and BO for TM-SPR<sub>Gaussian</sub> and TM-SPR<sub>Beta</sub>.**

	Whole-body CT Registration		Brain MRI Registration		Cardiac MRI Registration	
HyperMorph	$\lambda = 0.25$		$\lambda = 0.75$		$\lambda = 0.65$	
Hyper-TransMorph	$\lambda = 0.06$		$\lambda = 0.71$		$\lambda = 0.58$	
TM-SPR <sub>Gaussian</sub>	$\sigma' = 0.027$	$\lambda_{mean} = 0.991$	$\sigma' = 0.525$	$\lambda_{mean} = 3.796$	$\sigma' = 1.416$	$\lambda_{mean} = 1.094$
TM-SPR <sub>Beta</sub>	$\alpha' = 0.005$	$\lambda_{max} = 2.298$	$\alpha' = 0.175$	$\lambda_{max} = 3.354$	$\alpha' = 1.177$	$\lambda_{max} = 0.493$

2) *Quantitative Evaluation.* Table 3 presents the quantitative results for brain MRI registration. Optimization-based methods demonstrate strong performance for this task, with SyN achieving a mean Dice score of 0.758 and deedsBCV achieving 0.740. Notably, SyN significantly surpasses learning-based methods such as VoxelMorph and HyperMorph and performs comparably to TransMorph. It is worth mentioning that both VoxelMorph and HyperMorph were augmented with scaled-up model parameters, as suggested in recent research (Jian et al., 2024), yet SyN maintains robust performance. Its robust performance is likely due to the use of the "antsRegistrationSyN.sh" pipeline, specifically optimized for atlas-to-subject brain MRI registration, rather than the default registration pipeline used in our previous study (Chen et al., 2022b).

Among learning-based methods, TransMorph with a fixed regularization parameter ( $\lambda = 1$ ) outperforms both VoxelMorph and HyperMorph, with the latter optimized for regularization hyperparameters. Specifically, TransMorph achieves a mean Dice score of 0.757, compared to 0.744 for VoxelMorph and 0.753 for HyperMorph. When comparing hyperparameter learning methods, all approaches significantly outperform their backbone TransMorph. In particular, TM-SPR<sub>Gaussian</sub> achieves the highest mean Dice score of 0.767, closely followed by TM-SPR<sub>Beta</sub>, which also achieves 0.767 but with slightly higher variance, and Hyper-TransMorph at 0.762. The Wilcoxon signed-rank test reveals a significant difference between TM-SPR<sub>Gaussian</sub> and Hyper-TransMorph with  $p \ll 0.001$ .

Interestingly, the  $\lambda$  value for Hyper-TransMorph (0.58) is comparable to the  $\lambda_{max}$  value for TM-SPR<sub>Beta</sub> (0.493), as shown in Table 5. This indicates that the primary distinction between the two methods lies in their approach to regularization: Hyper-TransMorph applies a spatially-uniform regularization strength, while TM-SPR<sub>Beta</sub> employs spatially varying regularization. The superior mean Dice score achieved by TM-SPR<sub>Beta</sub> suggests that this improvement is attributable to the spatially varying, subject-adaptive deformation regularization, which facilitates a more precise alignment of brain structures.

A detailed comparison of Dice scores across various methods for different brain structures is illustrated using box plots in Fig. B.17 in the appendix.

In terms of deformation regularity, deedsBCV produced minor folded voxels and non-diffeomorphic volumes. As observed in the previous task, VoxelMorph and HyperMorph exhibit greater deformation irregularity. In contrast, TransMorph-based methods consistently produce highly regularized deformations.

### 5.3. Cardiac Image Registration Results on the ACDC and M&Ms Datasets

1) *Qualitative Evaluation.* The bottom row of Fig. 6 illustrates the qualitative results of cardiac MRI registration, with the middle panel showing results derived using the beta prior and the right panel showing results using the Gaussian prior. Unlike other tasks, the learned spatially varying regularization exhibits an almost piecewise constant pattern throughout the image, resulting in spatial weights that are large and nearly uniform across voxels. This observation is more pronounced with the beta prior, where the spatial weights appear more consistent.

Despite producing similar spatial weight volumes, it is important to note that the regularization imposed at each voxel differs between the two priors. Specifically, the Gaussian prior enforces relatively stronger regularization, as indicated by  $\lambda_{mean} = 1.094$  and  $\lambda_{max} = 0.493$ , shown in Table 5. Additional qualitative comparisons of various registration methods for the cardiac MRI registration task are presented in Fig. C.18 in the appendix.

2) *Quantitative Evaluation.* Table 4 presents the quantitative comparisons for this task. Among optimization-based methods, while SyN achieves a lower score of 0.678, deedsBCV achieves the highest mean Dice score of 0.740, outperforming all other methods, including learning-based approaches. This result indicates the superiority of deedsBCV for unsupervised image registration on cardiac MRI.

For learning-based baseline methods, consistent with other tasks, TransMorph, with a fixed regularization hyperparameter set to 1, outperforms both VoxelMorph and HyperMorph. Specifically, TransMorph achieves a mean Dice score of 0.711, compared to 0.689 for VoxelMorph and 0.647 for HyperMorph.

Notably, among methods that optimize regularization hyperparameters, Hyper-TransMorph underperforms its backbone, TransMorph, with a significantly lower mean Dice score of 0.698. Similarly, HyperMorph achieves lower performance compared to its backbone, VoxelMorph. In contrast, both TM-SPR<sub>Gaussian</sub> and TM-SPR<sub>Beta</sub> achieve significantly higher mean Dice scores of 0.733 and 0.735, respectively. These results indicate that the proposed method offers a more robust augmentation of the backbone model compared to spatially invariant regularization, resulting in significant performance improvements for this task.

A detailed comparison of Dice scores across various methods for the three cardiac structures is illustrated using box plots in Fig. C.19 in the appendix.

As observed in other tasks, all TransMorph-based models enforce diffeomorphism, resulting in highly regularized deformations with no folded voxels or non-diffeomorphic volumes.



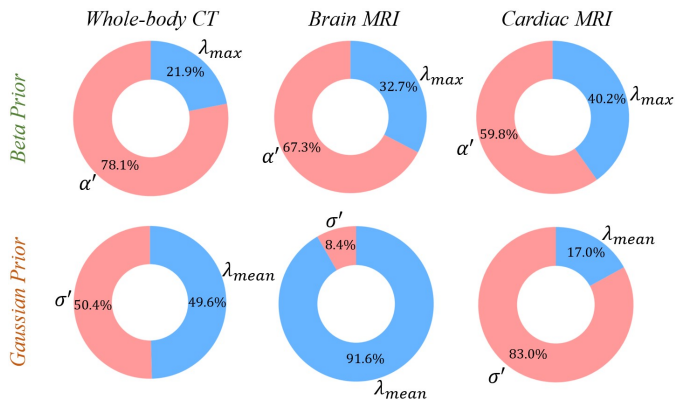


**Fig. 8.** The pie charts illustrate the contribution of hyperparameters for the proposed spatially varying regularization to registration performance, evaluated for two different prior types across three registration tasks.

This consistency highlights the robustness of these methods in producing anatomically plausible deformations.

## 6. Discussion

### 6.1. Hyperparameter Analysis

In the following subsections, we outline the hyperparameter search process for the baseline models, HyperMorph and Hyper-TransMorph, focusing on the regularization hyperparameter  $\lambda$ . Additionally, we detail the hyperparameter optimization process for the proposed spatially varying regularization method, emphasizing the selection of  $\alpha'$  and  $\sigma'$  to control the spatial coherence of the spatial weight volume ( $\lambda$ ), as well as  $\lambda_{max}$  and  $\lambda_{mean}$  to regulate the overall strength of the deformation regularization.

#### 6.1.1. Hyperparameter Selection for HyperMorph and Hyper-TransMorph

The hyperparameter learning framework introduced by HyperMorph enables the efficient determination of optimal regularization hyperparameters through a single training session. This approach involves inputting different hyperparameter values into the auxiliary network, which predicts the corresponding model parameters for the registration network. The best model parameters are then selected on the basis of the registration accuracy achieved in the validation set.

For this study, we performed a dense grid search for the optimal regularization hyperparameter  $\lambda$  within the range  $[0, 1]$ , using a step size of 0.01. The identified optimal  $\lambda$  values for both HyperMorph and Hyper-TransMorph across the three registration tasks are summarized in Table 5. Notably, the optimal  $\lambda$  values for brain and cardiac MRI registration tasks are similar for both models. However, for whole-body CT registration, Hyper-TransMorph favors a much smaller  $\lambda$  (0.06), indicating minimal or no regularization, whereas HyperMorph selects a relatively higher  $\lambda$  of 0.25, suggesting stronger regularization.

Figure D.20 in the appendix shows the dense grid search results. Although the overall trends in performance curves are consistent between the two models, with a sharp decline in performance observed beyond  $\lambda = 0.8$ , differences emerge in their peak

performance and the "turning points" where performance begins to drop significantly. Additionally, HyperMorph exhibits less variability in performance compared to Hyper-TransMorph. These differences suggest that the underlying network architecture significantly influences the optimal hyperparameter values, highlighting that the best hyperparameter setting for one deep learning architecture may not generalize well to others. Although further exploration of this observation is beyond the scope of this study, it opens an intriguing avenue for future research.

#### 6.1.2. Surface Maps for Different Prior Assumptions

Since the proposed framework uses Bayesian hyperparameter optimization to tune the newly introduced hyperparameters by maximizing the posterior probability, it avoids the relatively more time-consuming and less efficient grid search approach. Figure 7 illustrates surface maps of Dice scores in the validation set for different hyperparameters under distinct prior distributions, specifically,  $\lambda_{max}$  and  $\alpha'$  for the beta prior and  $\lambda_{mean}$  and  $\sigma'$  for the Gaussian prior. Cyan-edged scatter points indicate hyperparameters pruned during training, while black-edged points denote those that completed the full training process, with the red cross marking the optimal performance.

One immediately noticeable trend is that different datasets favor significantly different hyperparameters. Not only were the optimal values distinctly varied, even under the same prior assumption (as shown in Sect. 5), but the contour patterns themselves also differ substantially. Under the beta prior (top row in Fig. 7), whole-body CT image registration (autoPET) favored smaller  $\alpha'$  in the range  $[0, 0.02]$  and larger  $\lambda_{max}$  in the range  $[2, 3]$ . For brain registration, both  $\alpha'$  and  $\lambda_{max}$  were optimal at intermediate values, with  $\alpha'$  in the range  $[0.15, 0.2]$  and  $\lambda_{max}$  within  $[2, 3]$ . This led to spatial weights that were low in regions with greater structural differences (indicating less regularization) but consistently close to 1 elsewhere, enforcing strong regularization in these areas, as illustrated in Fig. 6. In contrast, cardiac image registration (ACDC M&Ms) preferred larger  $\alpha'$  values in the range  $[0.4, 0.6]$  and smaller  $\lambda_{max}$  values within  $[0.5, 2]$ , leading to spatial weights with a nearly constant high value of 1 across all voxels, as illustrated in Fig. 6.

A similar pattern appears under the Gaussian prior (bottom row in Fig. 7). For whole-body CT registration, large  $\lambda_{mean}$  values in the range  $[2, 3]$  and a small  $\sigma'$  close to 0 were favored. This is reflected in the qualitative results in Fig. 6, where the spatial weights are nearly zero within the body region. For brain registration, the preferred range for  $\sigma'$  was  $[0.5, 1.5]$ , with  $\lambda_{mean}$  within  $[3, 4]$ . Finally, for cardiac registration,  $\sigma'$  was preferred within  $[0.5, 1.25]$  and  $\lambda_{mean}$  within  $[1, 2]$ .

This variability in the surface maps underscores the necessity of dataset-specific hyperparameter tuning to achieve optimal performance across different tasks, supporting our assertion in the Introduction that different registration tasks favor spatially varying regularization differently at the voxel level. Consequently, no single universal set of hyperparameters is effective in all tasks.

#### 6.1.3. Hyperparameter Importance for Registration Accuracy

The contribution of each hyperparameter to the accuracy of the registration is assessed using functional ANOVA (fANOVA)

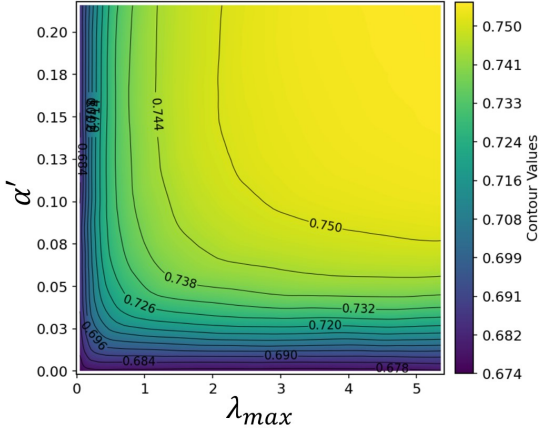


**Fig. 9.** Hyperparameter surface map for Hyper-TM-SPR<sub>Beta</sub>, illustrating the results of a dense grid search over  $\alpha'$  and  $\lambda_{max}$  and their impact on registration performance, as measured by Dice scores, for the brain MRI registration task (IXI).

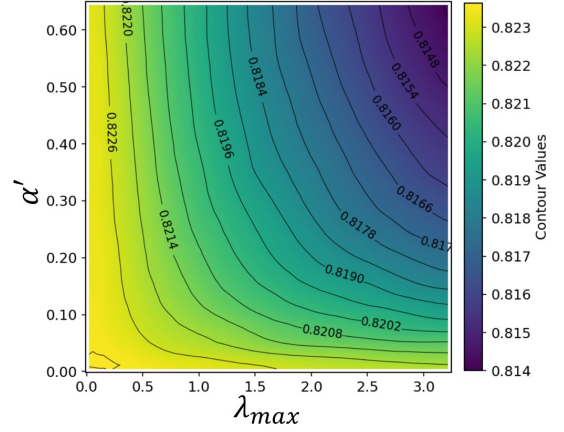


**Fig. 10.** Hyperparameter surface map for Hyper-TM-SPR<sub>Beta</sub>, illustrating the results of a dense grid search over  $\alpha'$  and  $\lambda_{max}$  and their impact on registration performance, as measured by Dice scores, for the cardiac MRI registration task (ACDC M&Ms).

from the Optuna package (Akiba et al., 2019). This sensitivity analysis technique examines how much registration performance (in our case, the Dice score) changes when each parameter is varied while the others are held constant, yielding a relative importance score for each hyperparameter that sums to 1.

The importance values for each registration task under two different prior assumptions are presented in Fig. 8. The results indicate that the importance of the hyperparameter varies depending on both the prior assumptions and the registration tasks, consistent with the trends observed in the surface maps. For the beta prior,  $\alpha'$ , which controls the spatial coherence of the spatial weight volume  $\lambda$ , exerts a greater influence on the registration performance than the per-voxel regularization strength  $\lambda_{max}$ . In contrast, for the Gaussian prior,  $\sigma'$  (which also controls spatial coherence) is less influential for brain registration on the IXI dataset than the per-voxel regularization strength  $\lambda_{mean}$ . However, for whole-body CT registration on the autoPET dataset,  $\sigma'$  and  $\lambda_{mean}$  are approximately equal importance.

## 6.2. Hyperparameter Learning for Spatially Varying Regularization

As this article introduces a novel deformation regularization strategy for image registration, our main focus was to rigorously evaluate the effects of the hyperparameters introduced on various registration tasks, with less emphasis on computational efficiency. As discussed earlier, the proposed method likely requires a unique set of optimal hyperparameters for different registration tasks, which poses a limitation due to the need for hyperparameter optimization for each application. Although we employed a more efficient BO approach for hyperparameter tuning, as opposed to a resource-intensive grid search, some level of optimization remains necessary for each specific registration task. Despite pruning many training trials before completing the full cycles, the model still needs to be trained from scratch multiple times during the optimization process.

In the following subsections, we demonstrate on the brain and cardiac MR image registration tasks how the proposed method can be seamlessly integrated within a hyperparameter learning

framework, using the concepts from HyperMorph (Hoopes et al., 2021). This setup requires only a single training cycle to enable continuous hyperparameter tuning, thereby avoiding potentially more computationally expensive (though more rigorous) hyperparameter optimization. For both tasks, we learn hyperparameters for spatially varying regularization under the beta prior (i.e., Hyper-TM-SPR<sub>Beta</sub>). To recap, the associated hyperparameters include 1)  $\alpha'$ , which controls the spatial coherence of the spatial weight volume  $\lambda$ , where larger values of  $\alpha'$  result in a more spatially uniform regularization strength throughout the image, and 2)  $\lambda_{max}$ , which represents the maximum regularization strength applied to a voxel, thereby influencing the overall regularization strength.

While hyperparameter learning facilitates continuous tuning of hyperparameters with fewer training cycles and reduced training times, it is not without limitations. Recent neural network architectures, such as Transformers (Zhai et al., 2022; Dehghani et al., 2023) or large-kernel ConvNets (Liu et al., 2022b; Ding et al., 2022; Woo et al., 2023), which rely on large model scales (i.e., a substantial number of trainable parameters), introduce significant computational challenges when used as the registration network within the hyperparameter learning framework. Specifically, the auxiliary network responsible for predicting the model parameters also scales up proportionally with the number of layers and parameters in the registration network.

As a result, while hyperparameter learning can potentially decrease the overall training time, the computational demands for a single training cycle are considerably high. For instance, in the case of Hyper-TM-SPR applied to brain MRI registration, the training process required over 70 GB of GPU memory, presenting a significant challenge in practical applications. Although redesigning the auxiliary network to be more memory efficient is possible, it is beyond the scope of this study. This challenge further justify our choice of BO, which retains the same computational demands as running the original registration network, which for the same TM-SPR required less than 20 GB of memory.

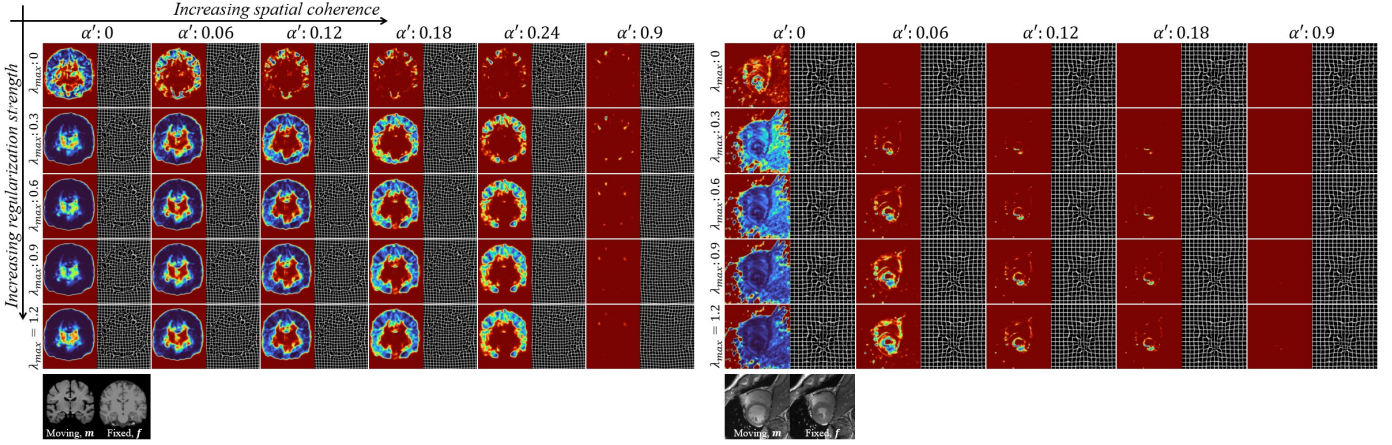


**Fig. 11.** Visualization of spatial weight volumes and corresponding deformation fields through continuous tuning of the hyperparameters ( $\alpha'$  and  $\lambda_{max}$ ) using the hyperparameter learning method applied to the proposed spatially varying regularization (i.e., Hyper-TM-SPR $_{Beta}$ ). The left panel presents results from brain MRI registration (IXI), while the right panel shows results from cardiac MRI registration (ACDC M&Ms). For the cardiac MRI task, anatomical label maps were incorporated during training to demonstrate the proposed method's applicability to semi-supervised or supervised registration tasks.

**Table 6.** Quantitative results for hyperparameter learning applied to the proposed spatially varying regularization under the beta prior (denoted as Hyper-TM-SPR $_{Beta}$ ), compared to models without hyperparameter learning. Results for models without hyperparameter learning are taken from Table 3 and Table 4. For cardiac MRI registration, anatomical label maps was incorporated during training for Hyper-TM-SPR $_{Beta}$ .

Brain MRI Registration (IXI)			
Method	Dice $\uparrow$	% $ J  \leq 0 \downarrow$	%NDV $\downarrow$
TM-SPR $_{Beta}$	0.767 $\pm$ 0.129	0.00%	0.00%
Hyper-TM-SPR $_{Beta}$	0.762 $\pm$ 0.127	0.00%	0.00%
Cardiac MRI Registration (ACDC M&Ms)			
Method	Dice $\uparrow$	% $ J  \leq 0 \downarrow$	%NDV $\downarrow$
TM-SPR $_{beta}$	0.735 $\pm$ 0.119	0.00%	0.00%
Hyper-TM-SPR $_{Beta}$	0.848 $\pm$ 0.091	0.00%	0.03%

### 6.2.1. Unsupervised Registration

We first demonstrate the application of hyperparameter learning for spatially varying regularization in the brain MRI registration task within an unsupervised learning framework. Similar to the baseline models HyperMorph and Hyper-TransMorph, we employed an auxiliary network composed of fully connected subnetworks to predict the model parameters for TM-SPR $_{Beta}$  based on the input hyperparameters, represented as a vector containing two scalars:  $\alpha'$  and  $\lambda_{max}$ . The maximum values for  $\alpha'$  and  $\lambda_{max}$  sampled during training were set to match those used in the previously performed BO, specifically 0.2 for  $\alpha'$  and 5 for  $\lambda_{max}$ . During training, the input values to the auxiliary network were normalized by these maximum values. All other training settings remained consistent with the original TM-SPR $_{Beta}$ . This new model is denoted as Hyper-TM-SPR $_{Beta}$  to emphasize its hyperparameter learning capability.

After training, different values of  $\alpha'$  and  $\lambda_{max}$  were continuously sampled to assess their impact on the generated spatial weight volumes and the associated deformation fields. The left panel of Fig. 11 illustrates these spatial weight volumes and

deformation fields for an example image pair, demonstrating the effects of varying hyperparameters. For a fixed  $\lambda_{max}$ , increasing  $\alpha'$  from 0 to 0.9 results in greater spatial coherence within the spatial weight volume, approaching uniform values throughout the image. This observation aligns with theoretical expectations, as the weight of the penalty term (Eqn. 18) that enforces higher spatial weights increases with  $\alpha'$ . On the other hand, when  $\alpha'$  is fixed and  $\lambda_{max}$  increases from 0 to 1.2, a different trend is observed. Larger  $\lambda_{max}$  values, corresponding to stronger regularization, lead to lower spatial weights in specific regions. For example, at  $\lambda_{max} = 0$ , only a small portion of the cortical regions is assigned lower spatial weights (indicated by blue regions). As  $\lambda_{max}$  increases to 1.2, these regions and their surroundings exhibit progressively darker shades of blue, reflecting further reductions in spatial weights.

This empirical observation suggests that, while increasing  $\lambda_{max}$  imposes a stronger overall regularization by setting a larger upper bound, it also decreases spatial weights, potentially counteracting the intended effect. *To effectively enforce stronger regularization across the entire image, both  $\lambda_{max}$  and  $\alpha'$  need to be increased simultaneously, moving diagonally in the hyperparameter space.*

We also performed a dense grid search for  $\alpha'$  and  $\lambda_{max}$  with step sizes of 0.004 and 0.1, respectively, to generate a surface map of Dice scores on the validation data set. The resulting surface map, shown in Fig. 9, aligns visually with the surface map obtained using BO (Fig. 7) for the beta prior on the same dataset. Specifically, the task favors larger values for both  $\alpha'$  and  $\lambda_{max}$ , with the optimal values determined to be 0.212 and 5.4, respectively, which differ slightly from the BO-derived optimal values listed in Table 5. The quantitative comparison between Hyper-TM-SPR $_{Beta}$  and TM-SPR $_{Beta}$  (optimized with BO) is presented in Table 6. While Hyper-TM-SPR $_{Beta}$  achieves a slightly lower mean Dice score of 0.762 compared to 0.767 for TM-SPR $_{Beta}$ , the difference is statistically significant, as determined by the Wilcoxon signed-rank test. These results suggest that, while hyperparameter learning is effective for exploring



a range of hyperparameter values and is computationally more efficient, BO remains preferable for identifying the optimal hyperparameter values and achieving the best-performing model.

### 6.2.2. Semi-supervised Registration

We next investigate the applicability of the proposed spatially varying regularization for semi-supervised image registration, a widely used approach that incorporates label map supervision during training to enhance registration performance (Chen et al., 2025). This is demonstrated on the cardiac registration task, as it is the only task where learning-based models did not outperform the optimization-based method, as shown in Table 4. Semi-supervised learning provides a distinct advantage for learning-based approaches by leveraging available anatomical label maps to guide the learning process, offering an opportunity to improve registration performance. Furthermore, we demonstrate that the proposed spatially varying regularization is not limited to unsupervised learning but can also be seamlessly integrated into semi-supervised registration frameworks.

The hyperparameter learning framework largely follows the approach described in Sect. 6.2.1, with the primary difference being the inclusion of an additional loss term. Specifically, a Dice loss is introduced to compare the anatomical label map of the deformed moving image to that of the fixed image. This Dice loss is added to Eqn. 19, with its weight set equal to that of the image similarity measure, both assigned a value of 1. The hyperparameter values of  $\alpha'$  and  $\lambda_{max}$  are provided as input to the auxiliary network, which predicts the model parameters for the registration network. The maximum values for  $\alpha'$  and  $\lambda_{max}$  were set to 0.6 and 3, respectively. Similarly to the unsupervised learning setup in Sect. 6.2.1, the sampled hyperparameter values were normalized by their maximum values before being input into the network.

The right panel of Fig. 11 shows the spatial weight volumes and their associated deformation fields obtained for a sample cardiac MRI image pair using various  $\alpha'$  and  $\lambda_{max}$  values. Despite the additional Dice loss during training, the trends observed are consistent with those in the unsupervised learning task described in Sect. 6.2.1. Specifically, increasing  $\alpha'$  promotes greater spatial uniformity within the spatial weights in the image domain. In contrast, increasing  $\lambda_{max}$ , which raises the maximum regularization strength applied to individual voxel locations, results in smaller spatial weights in specific regions.

To further investigate the relationship between hyperparameters and registration performance, we performed a dense grid search for  $\alpha'$  and  $\lambda_{max}$  with step sizes of 0.012 and 0.06, respectively, and generated hyperparameter surface maps based on Dice scores, as shown in Fig. 10. Interestingly, these surface maps differ from those obtained by BO for the unsupervised learning task on cardiac MRI registration (as shown in Fig. 7). Specifically, the surface maps for the semi-supervised task favor smaller values for both  $\alpha'$  and  $\lambda_{max}$ , with the optimal values identified as 0.012 and 0.12, respectively, indicating a bias towards minimal regularization. In contrast, the unsupervised task favors relatively larger values for both  $\alpha'$  and  $\lambda_{max}$ .

This discrepancy likely arises from the bias introduced by the Dice loss during training. Since the surface maps were gener-

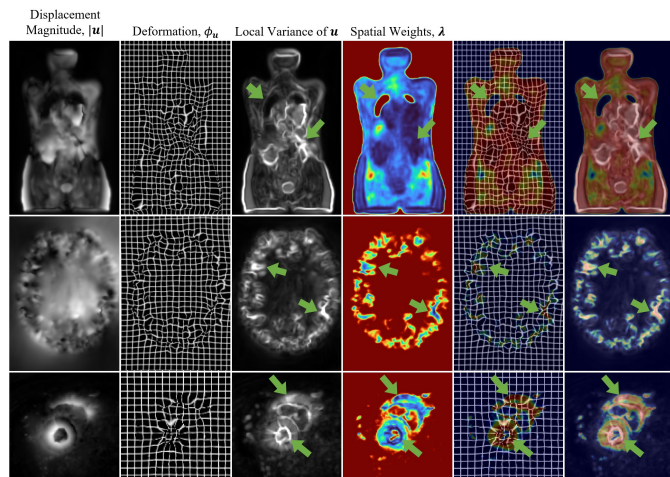


**Fig. 12.** Visualization of spatial weight volumes and deformation fields, highlighting their correlation for improved interpretability. From left to right, the images depict: displacement magnitude, deformation field, local variance map, spatial weight volume, and spatial weight volume overlaid on the deformation field and local variance map (both with inverted colormaps for the spatial weight volume).

ated using Dice as the performance metric, the regularization inherently skews towards optimizing Dice alone, potentially reducing the influence of regularization. However, the resulting deformation fields remain smooth and almost free of folding, as indicated by "%|J| ≤ 0" and "%NDV" values in Table 6, due to the enforcement of diffeomorphic registration.

This finding underscores a critical consideration: *When applying the proposed method to semi-supervised tasks where diffeomorphic constraints are not imposed but Dice loss is used during training, relying solely on Dice as the success metric may lead to small hyperparameter values that impose weak to minimal regularization strength at each voxel location, potentially resulting in nonsmooth deformations that are often undesirable. As Dice is often considered a surrogate measure of registration performance (Rohlfing, 2011), completely abandoning smoothness constraints may exacerbate true registration errors.*

It is worth noting, however, that the proposed method can be extended beyond Dice loss for label map matching. For instance, target registration errors, often considered the gold standard for registration accuracy, can be incorporated as an auxiliary loss function in place of Dice loss within the proposed spatially varying regularization framework when landmarks are available for training.

In terms of quantitative evaluation, Table 6 shows that Hyper-TM-SPR<sub>Beta</sub>, using the optimal hyperparameter values determined by grid search, achieved a significantly higher mean Dice score of 0.848, as measured by the Wilcoxon signed-rank test ( $p$ -values  $\ll 0.001$ ), compared to the unsupervised learning model TM-SPR<sub>Beta</sub>, which achieved 0.735. Furthermore, Hyper-TM-SPR<sub>Beta</sub> outperformed the best performing optimization-based method for the cardiac MRI registration task, deedsBCV, which achieved a mean Dice score of 0.740.



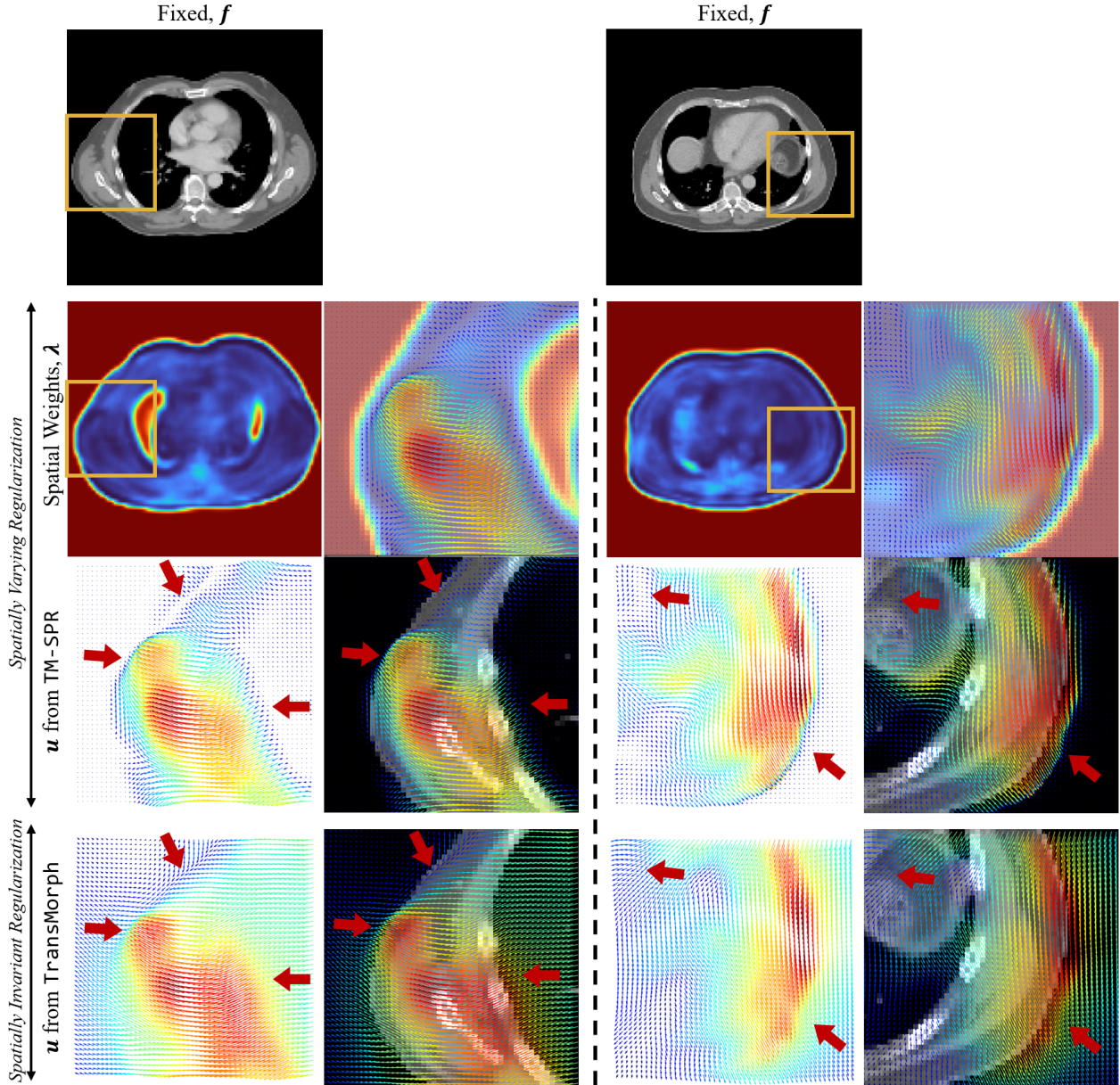


**Fig. 13.** Visualization of the spatial weight volume and the corresponding displacement fields generated by the proposed spatially varying regularization (TM-SPR, top and middle rows), compared to the displacement fields produced by spatially invariant regularization (TransMorph, bottom row). The spatially varying regularization inherently introduces controlled discontinuities in the displacement field to better adapt to local image features.

### 6.3. Explainable Image Registration

Deep learning models are often perceived as "black boxes," lacking interpretability in their predictions, particularly in how they estimate deformation fields from input image pairs. Efforts to address this limitation for image registration have typically focused on exploring interpretability through various approaches, including examining registration uncertainty (Chen et al., 2025, 2024; Dalca et al., 2019b; Luo et al., 2019), leveraging attention maps derived from self- or cross-attention mechanisms in attention-based models (Shi et al., 2022; Chen et al., 2023b; Liu et al., 2024b), and leveraging activation maps generated through methods such as gradient-weighted class activation mapping (Grad-CAM) (Selvaraju et al., 2017; Chen et al., 2023b).

In this work, the proposed spatially varying regularization, facilitated by the spatial weight volume, introduces a novel framework for interpreting learning-based image registration, complementing existing approaches. The spatial weight volume offers valuable insights into how the deep learning model derives the deformation field. As described in Sect. 3.2, the spatial weight volume is intrinsically linked to the covariance of the displacement field, conditioned on the input images. This relationship effectively captures the complexity of the deformation field by indicating regions where stricter deformation control (higher spatial weights) or looser control (lower spatial weights) is preferred.

As shown in Fig. 12 and indicated by the arrows, the spatial

weight volume serves as a practical tool to understand how the model adjusts the deformation control to optimize registration performance. Regions with minimal structural differences between moving and fixed images, such as the background or inner lung regions, are assigned high spatial weights to suppress unnecessary deformations. In contrast, regions that require complex deformations, such as the cortical areas in brain images or the edges of cardiac structures, are assigned lower spatial weights, allowing the flexibility needed to accommodate intricate deformations.

However, it is important to note that the interpretability of the spatial weight volume diminishes if the hyperparameter controlling its spatial coherence is set too high. Excessive coherence results in near-uniform values across the entire image, reducing the association between the spatial weight volume and the complexity of the deformation field, thereby limiting its utility as an interpretability tool.

#### 6.4. Adaptive Regularization

Prior work has demonstrated that different registration tasks or patient cohorts may require substantially different regularization strengths (Simpson *et al.*, 2012). However, existing learning-based methods often lack the ability to produce adaptive regularization specific to a given input image pair. Instead, regularization strength is typically pre-determined before training and remains fixed once the model is trained. Adjusting the regularization strength after training requires retraining the entire registration network from scratch. Although hyperparameter learning methods, such as HyperMorph (Hoopes *et al.*, 2021), allow for test-time adjustment of hyperparameters, the regularization itself remains non-adaptive and requires manual tuning for each specific image pair.

In contrast, the proposed spatially varying regularization is inherently adaptive and tailored to each pair of images. While it involves two tunable hyperparameters—controlling the maximum regularization strength in the case of the beta prior, or the mean regularization strength in the case of the Gaussian prior, as well as the expected degree of spatial variation—these hyperparameters govern the framework rather than the specific regularization applied. The actual regularization strength is adaptively predicted for each image pair during the registration process, allowing a more flexible and precise alignment tailored to the given data.

Moreover, the proposed framework is designed to integrate seamlessly with most existing learning-based registration methods. With only minor modifications to the network architecture to incorporate a lightweight module for estimating the spatial weight volume, as well as an adaptable loss function compatible with various image similarity measures and deformation regularization strategies, this method offers a highly versatile enhancement to augment learning-based image registration.

#### 6.5. Discontinuity-Preserving Registration

Discontinuity-preserving image registration has been an important focus in medical image registration research. This is motivated by the observation that deformations in the human body do not always follow continuous motion assumptions. At

certain anatomical boundaries, discontinuous motion can occur, such as a sliding motion in which adjacent structures move in opposite directions. Traditional global smoothing regularizers, such as the diffusion regularizer, are not well-suited to handle such scenarios. To address this limitation, previous studies have proposed modifications to the regularizer formulation, such as anisotropic diffusion regularization (Pace *et al.*, 2013), or adaptations to the registration framework that explicitly accommodate discontinuities in the deformation field (Zheng *et al.*, 2024; Chen *et al.*, 2021b).

The proposed spatially varying regularization inherently supports discontinuities in the deformation field, while still accommodating diffeomorphic constraints when required. This is achieved through the spatial weight volume, which assigns varying regularization strengths across the image. By assigning near-zero spatial weights at anatomical boundaries, the method effectively allows for sudden changes or discontinuous displacements in these regions. Even under diffeomorphic registration, this behavior can still be approximated. As illustrated in Fig. 13, the proposed TM-SPR framework enables sharper transitions in displacements at anatomical boundaries, as highlighted by the red arrows. In regions exhibiting these sharper transitions, the corresponding spatial weights are notably low, appearing darker in the spatial weight volume. In contrast, the spatially invariant regularization used by TransMorph produces globally smooth displacements, which limits its ability to capture such transitions. Importantly, both methods employ a time-stationary framework, ensuring that the resulting deformations are diffeomorphic despite the sharper changes observed with TM-SPR.

Compared to existing regularizer-based approaches that handle discontinuities, the proposed method offers a clear advantage by adaptively learning the regularization strength directly from the data. Furthermore, discontinuities can be fully suppressed by enforcing spatial uniformity in the spatial weight volume, making the method highly flexible and adaptable to varying registration tasks.

## 7. Conclusion

In this study, we introduced an end-to-end, unsupervised framework for learning spatially varying regularization in medical image registration. Unlike existing learning-based methods that typically rely on spatially invariant regularization, the proposed approach generates a spatial weight volume that assigns individual weights to voxels, enabling spatially adaptive regularization. We also proposed a novel loss function formulation that incorporates two hyperparameters designed to compel the network to apply stronger regularization based on a specified maximum or mean regularization strength. Additionally, we introduced efficient hyperparameter tuning methods through Bayesian optimization and hyperparameter learning strategies to allow adjustment of these parameters during the test time.

The effectiveness of the proposed framework was demonstrated on three publicly available datasets that encompass diverse registration tasks and anatomical regions. Both qualitative and quantitative results highlight the advantages of the spatially varying regularization framework, positioning it as a valuable

complement to existing learning-based medical image registration methods.

### **Acknowledgments**

Junyu Chen and Yong Du were supported by grants from the National Institutes of Health (NIH), United States, P01-CA272222 (PI: G. Sgouros), R01-EB031023 (PI: Y. Du), and U01-EB031798 (PI: G. Sgouros). Shuwen Wei, Yihao Liu, and Aaron Carass were supported by the NIH from National Eye Institute grants R01-EY024655 (PI: J.L. Prince) and R01-EY032284 (PI: J.L. Prince), as well as the National Science Foundation grant 1819326 (Co-PI: S. Scott, Co-PI: A. Carass). Harrison Bai was supported by the NIH from National Cancer Institute grant R03-CA286693 (Co-PI: B. Kimia, Co-PI: H. Bai). The views expressed in written conference materials or publications and by speakers and moderators do not necessarily reflect the official policies of the NIH; nor does mention by trade names, commercial practices, or organizations imply endorsement by the U.S. Government.



**Appendix A. Additional Qualitative and Quantitative Results for Whole-body CT Registration Task**

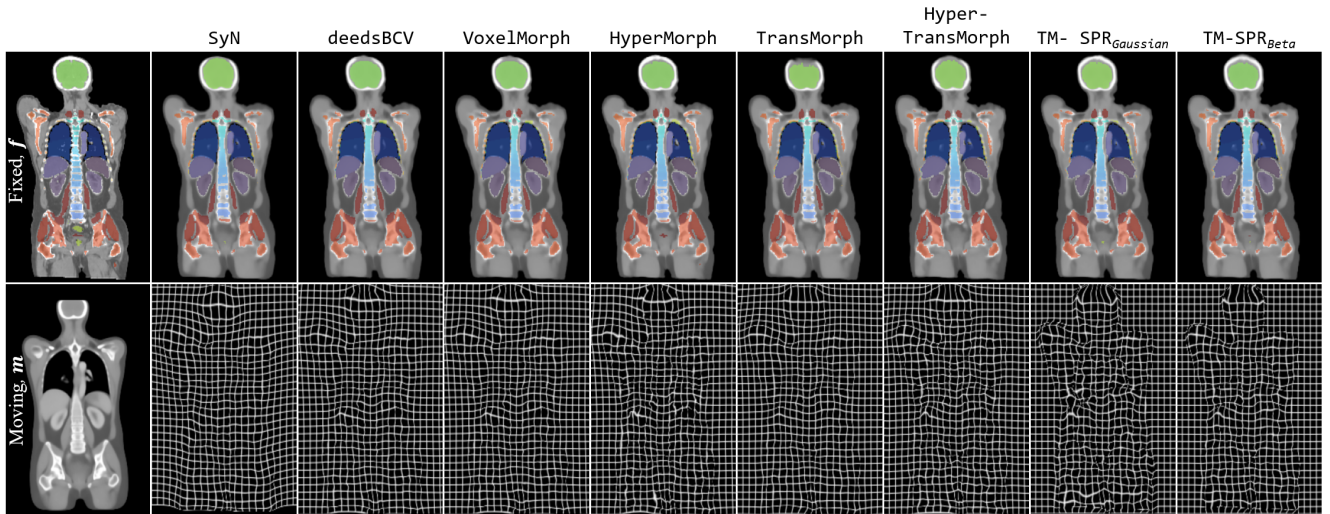


**Fig. A.14. Qualitative comparison of registration methods for whole-body CT registration on the *autoPET* dataset.**

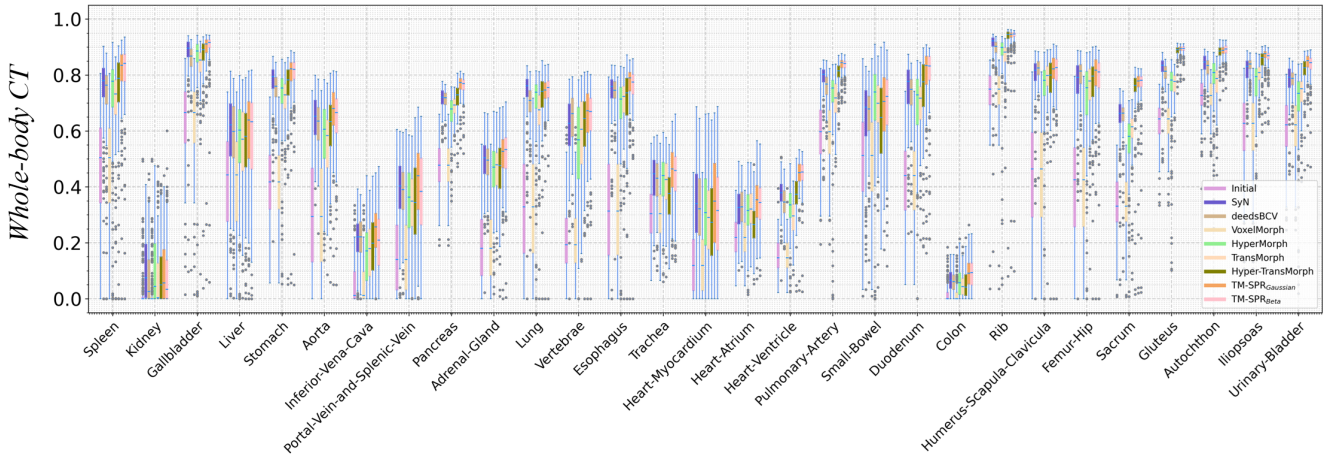


**Fig. A.15. Quantitative comparison of registration methods for whole-body CT registration on the *autoPET* dataset. Boxplots illustrate the Dice scores achieved for different organs in CT images.**



## Appendix B. Additional Qualitative and Quantitative Results for Brain MRI Registration Task

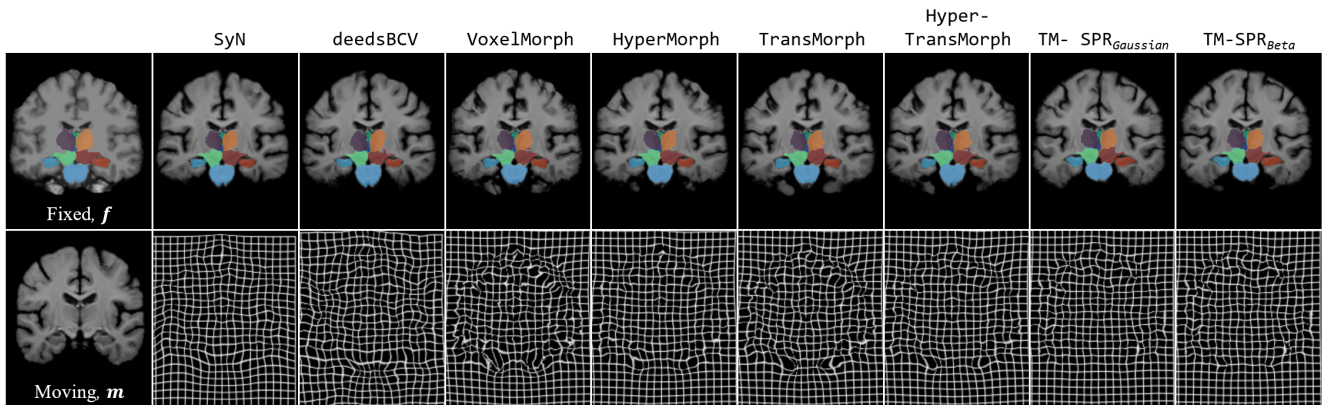


Fig. B.16. Qualitative comparison of registration methods for brain MRI registration on the IXI dataset.

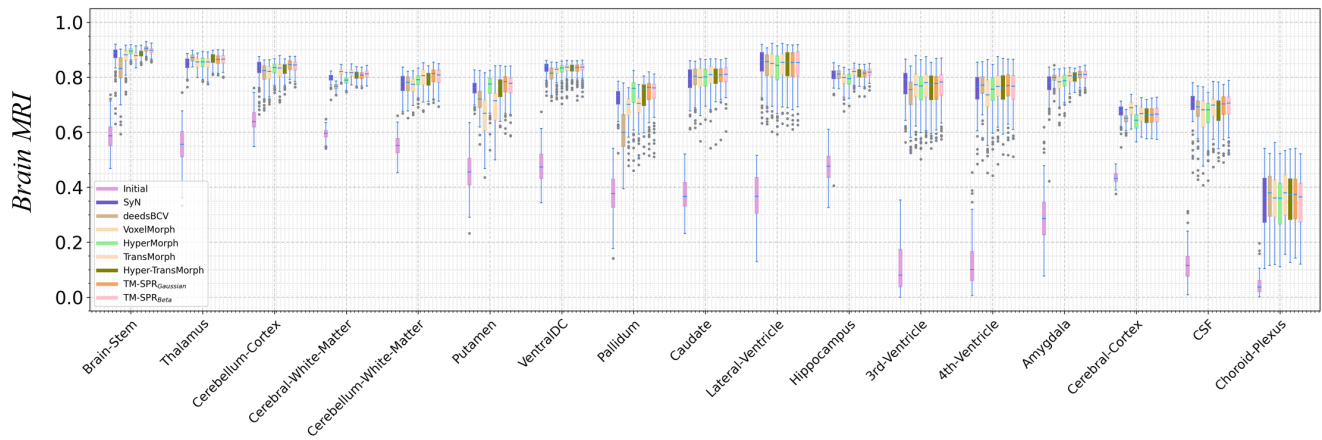


Fig. B.17. Quantitative comparison of registration methods for brain MRI registration on the IXI dataset. Boxplots illustrate the Dice scores achieved for different brain structures in MRI images.

## Appendix C. Additional Qualitative and Quantitative Results for Cardiac MRI Registration Task

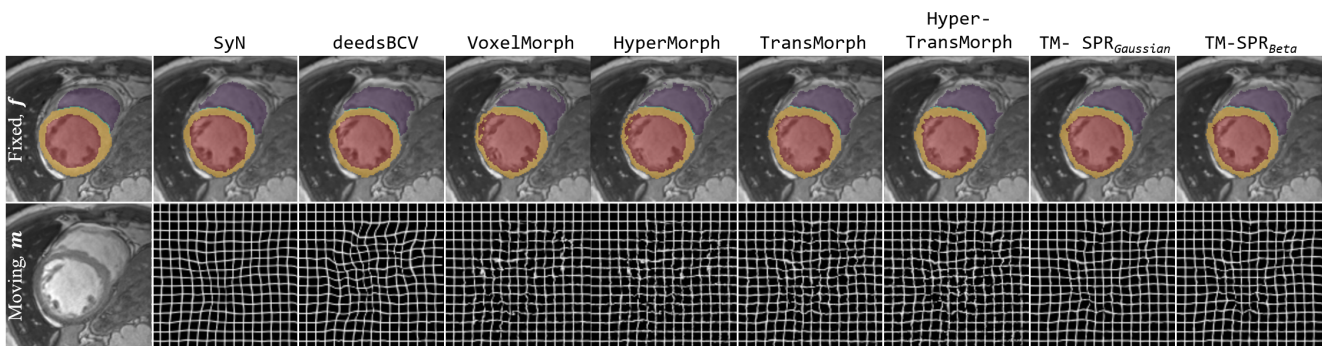


Fig. C.18. Qualitative comparison of registration methods for cardiac MRI registration on the ACDC and M&Ms dataset.

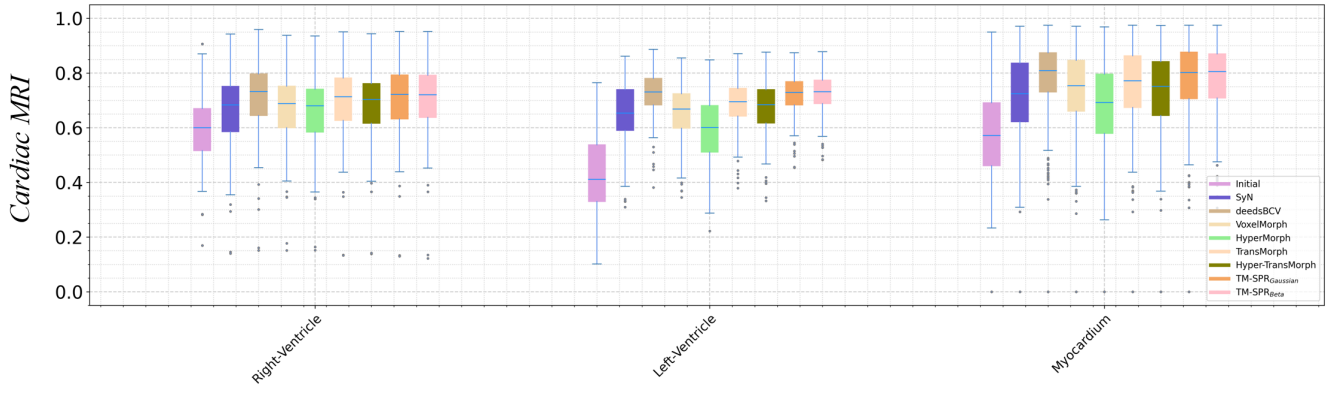


Fig. C.19. Quantitative comparison of registration methods for cardiac MRI registration on the *ACDC* and *M&Ms* dataset. Boxplots illustrate the Dice scores achieved for different cardiac structures in MRI images.

Appendix D. Hyperparameter Landscape for HyperMorph and Hyper-TransMorph

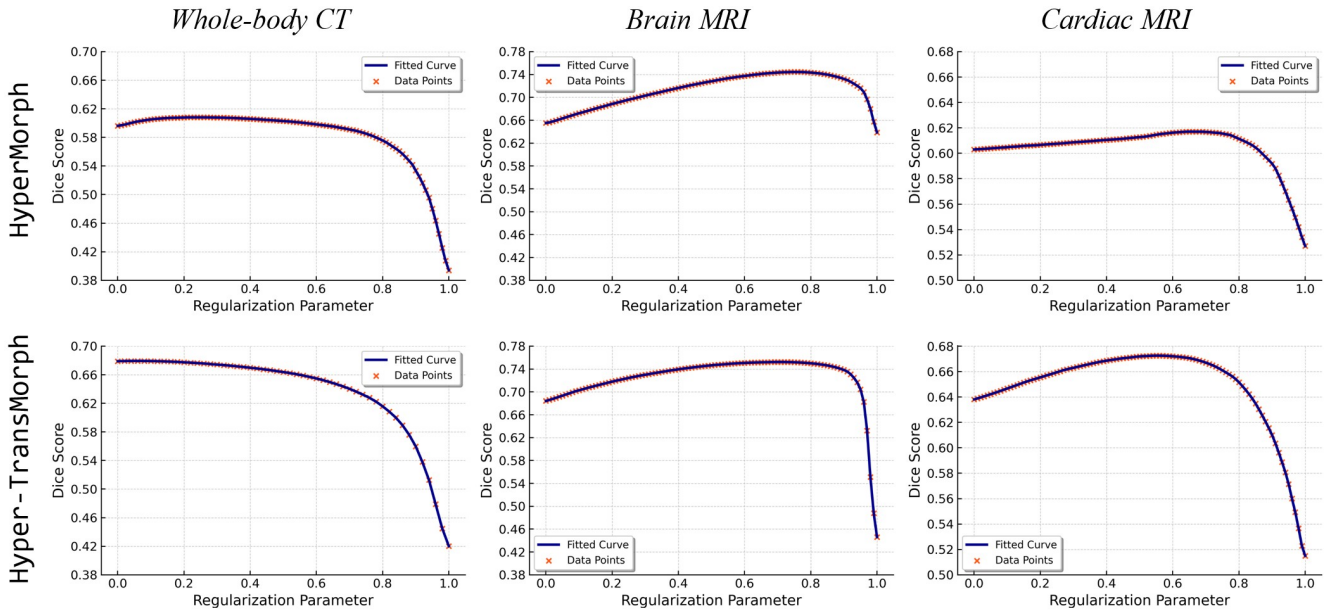


Fig. D.20. The plots show the grid search results for the regularization hyperparameter (with a step size of 0.01) and its impact on registration performance, as measured by Dice scores. The top row corresponds to HyperMorph, while the bottom row corresponds to Hyper-TransMorph, evaluated across the three registration tasks.

## References

- Akiba, T., Sano, S., Yanase, T., Ohta, T., Koyama, M., 2019. Optuna: A next-generation hyperparameter optimization framework, in: Proceedings of the 25th ACM SIGKDD international conference on knowledge discovery & data mining, pp. 2623–2631.
- Arsigny, V., Commowick, O., Pennec, X., Ayache, N., 2006. A log-euclidean framework for statistics on diffeomorphisms, in: 9<sup>th</sup> International Conference on Medical Image Computing and Computer Assisted Intervention (MICCAI 2006), Springer. pp. 924–931.
- Ashburner, J., 2007. A fast diffeomorphic image registration algorithm. *Neuroimage* 38, 95–113.
- Avants, B.B., Epstein, C.L., Grossman, M., Gee, J.C., 2008. Symmetric diffeomorphic image registration with cross-correlation: evaluating automated labeling of elderly and neurodegenerative brain. *Medical image analysis* 12, 26–41.
- Avants, B.B., Tustison, N., Song, G., et al., 2009. Advanced normalization tools (ANTS). *Insight j* 2, 1–35.
- Balakrishnan, G., Zhao, A., Sabuncu, M.R., Guttag, J., Dalca, A.V., 2019. Voxelmorph: a learning framework for deformable medical image registration. *IEEE Trans. Med. Imag.* 38, 1788–1800.
- Beg, M.F., Miller, M.I., Trounev, A., Younes, L., 2005. Computing large deformation metric mappings via geodesic flows of diffeomorphisms. *International journal of computer vision* 61, 139–157.
- Bergstra, J., Bardenet, R., Bengio, Y., Kégl, B., 2011. Algorithms for hyperparameter optimization. *Advances in neural information processing systems* 24.
- Bernard, O., Lalonde, A., Zotti, C., Cervenansky, F., Yang, X., Heng, P.A., Cetin, I., Lekadir, K., Camara, O., Ballester, M.A.G., et al., 2018. Deep learning techniques for automatic mri cardiac multi-structures segmentation and diagnosis: is the problem solved? *IEEE Trans. Med. Imag.* 37, 2514–2525.
- Campello, V.M., Gkontra, P., Izquierdo, C., Martín-Isla, C., Sojoudi, A., Full, P.M., Maier-Hein, K., Zhang, Y., He, Z., Ma, J., et al., 2021. Multi-centre, multi-vendor and multi-disease cardiac segmentation: the M&Ms challenge. *IEEE Trans. Med. Imag.* 40, 3543–3554.
- Chen, J., Frey, E.C., Du, Y., 2022a. Unsupervised Learning of Diffeomorphic Image Registration via TransMorph, in: International Workshop on Biomedical Image Registration, Springer. pp. 96–102.
- Chen, J., Frey, E.C., He, Y., Segars, W.P., Li, Y., Du, Y., 2022b. Transmorph: Transformer for unsupervised medical image registration. *Medical Image Analysis* 82, 102615.
- Chen, J., He, Y., Frey, E., Li, Y., Du, Y., 2021a. ViT-V-Net: Vision Transformer for Unsupervised Volumetric Medical Image Registration, in: *Medical Imaging with Deep Learning*, pp. 1–3.
- Chen, J., Leal, J., Rowe, S., Pomper, M., Du, Y., 2023a. Constructing PET/CT Atlas for PSMA Dosimetry.
- Chen, J., Liu, Y., He, Y., Du, Y., 2023b. Deformable cross-attention transformer for medical image registration, in: International Workshop on Machine Learning in Medical Imaging, Springer. pp. 115–125.
- Chen, J., Liu, Y., Wei, S., Bian, Z., Carass, A., Du, Y., 2024. From Registration Uncertainty to Segmentation Uncertainty, in: 21<sup>th</sup> International Symposium on Biomedical Imaging (ISBI 2024), pp. 1–5.
- Chen, J., Liu, Y., Wei, S., Bian, Z., Subramanian, S., Carass, A., Prince, J.L., Du, Y., 2025. A survey on deep learning in medical image registration: New technologies, uncertainty, evaluation metrics, and beyond. *Medical Image Analysis* 100, 103385.
- Chen, X., Xia, Y., Ravikumar, N., Frangi, A.F., 2021b. A deep discontinuity-preserving image registration network, in: 24<sup>th</sup> International Conference on Medical Image Computing and Computer Assisted Intervention (MICCAI 2021), Springer. pp. 46–55.
- Dalca, A., Rakic, M., Guttag, J., Sabuncu, M., 2019a. Learning conditional deformable templates with convolutional networks. *Advances in neural information processing systems* 32.
- Dalca, A.V., Balakrishnan, G., Guttag, J., Sabuncu, M.R., 2019b. Unsupervised learning of probabilistic diffeomorphic registration for images and surfaces. *Medical Image Analysis* 57, 226–236.
- Dehghani, M., Djolonga, J., Mustafa, B., Padlewski, P., Heek, J., Gilmer, J., Steiner, A.P., Caron, M., Geirhos, R., Alabdulmohsin, I., et al., 2023. Scaling vision transformers to 22 billion parameters, in: International Conference on Machine Learning, PMLR. pp. 7480–7512.
- Ding, X., Zhang, X., Han, J., Ding, G., 2022. Scaling up your kernels to 31x31: Revisiting large kernel design in cnns, in: 2022 IEEE Conference on Computer Vision and Pattern Recognition (CVPR), pp. 11963–11975.
- Fischl, B., 2012. FreeSurfer. *Neuroimage* 62, 774–781.
- Gatidis, S., Hepp, T., Früh, M., La Fougère, C., Nikolaou, K., Pfannenber, C., Schölkopf, B., Küstner, T., Cyran, C., Rubin, D., 2022. A whole-body FDG-PET/CT Dataset with manually annotated Tumor Lesions. *Scientific Data* 9, 601.
- Gerig, T., Shahim, K., Reyes, M., Vetter, T., Lüthi, M., 2014. Spatially varying registration using Gaussian processes, in: 17<sup>th</sup> International Conference on Medical Image Computing and Computer Assisted Intervention (MICCAI 2014), Springer. pp. 413–420.
- Heinrich, M.P., Jenkinson, M., Bhushan, M., Matin, T., Gleeson, F.V., Brady, M., Schnabel, J.A., 2012. MIND: Modality independent neighbourhood descriptor for multi-modal deformable registration. *Medical Image Analysis* 16, 1423–1435.
- Heinrich, M.P., Jenkinson, M., Brady, M., Schnabel, J.A., 2013. MRF-based deformable registration and ventilation estimation of lung CT. *IEEE Trans. Med. Imag.* 32, 1239–1248.
- Hoffmann, M., Billot, B., Greve, D.N., Iglesias, J.E., Fischl, B., Dalca, A.V., 2021. SynthMorph: learning contrast-invariant registration without acquired images. *IEEE Trans. Med. Imag.* 41, 543–558.
- Hoopes, A., Hoffmann, M., Fischl, B., Guttag, J., Dalca, A.V., 2021. Hypermorph: Amortized hyperparameter learning for image registration, in: International Conference on Information Processing in Medical Imaging, Springer. pp. 3–17.
- Hoopes, A., Hoffmann, M., Greve, D.N., Fischl, B., Guttag, J., Dalca, A.V., 2022. Learning the effect of registration hyperparameters with hypermorph. *The journal of machine learning for biomedical imaging* 1.
- Jian, B., Pan, J., Ghahremani, M., Rueckert, D., Wachinger, C., Wiestler, B., 2024. Mamba? Catch The Hype Or Rethink What Really Helps for Image Registration, in: International Workshop on Biomedical Image Registration, Springer. pp. 86–97.
- Kabus, S., Franz, A., Fischer, B., 2006. Variational image registration with local properties, in: International Workshop on Biomedical Image Registration, Springer. pp. 92–100.
- Kim, B., Kim, D.H., Park, S.H., Kim, J., Lee, J.G., Ye, J.C., 2021. CycleMorph: cycle consistent unsupervised deformable image registration. *Medical Image Analysis* 71, 102036.
- Kingma, D.P., Ba, J., 2014. Adam: A method for stochastic optimization. *arXiv preprint arXiv:1412.6980*.
- Liu, Y., Chen, J., Wei, S., Carass, A., Prince, J.L., 2024a. On Finite Difference Jacobian Computation in Deformable Image Registration. *International Journal of Computer Vision* 132, 3678–3688.
- Liu, Y., Chen, J., Zuo, L., Carass, A., Prince, J.L., 2024b. Vector field attention for deformable image registration. *Journal of Medical Imaging* 11, 064001–064001.
- Liu, Y., Zuo, L., Han, S., Xue, Y., Prince, J.L., Carass, A., 2022a. Coordinate translator for learning deformable medical image registration, in: International Workshop on Multiscale Multimodal Medical Imaging, Springer. pp. 98–109.
- Liu, Z., Lin, Y., Cao, Y., Hu, H., Wei, Y., Zhang, Z., Lin, S., Guo, B., 2021. Swin transformer: Hierarchical vision transformer using shifted windows, in: 2021 IEEE Conference on Computer Vision and Pattern Recognition (CVPR), pp. 10012–10022.
- Liu, Z., Mao, H., Wu, C.Y., Feichtenhofer, C., Darrell, T., Xie, S., 2022b. A convnet for the 2020s, in: 2022 IEEE Conference on Computer Vision and Pattern Recognition (CVPR), pp. 11976–11986.
- Luo, J., Sedghi, A., Popuri, K., Cobzas, D., Zhang, M., Preiswerk, F., Toews, M., Golby, A., Sugiyama, M., Wells, W.M., et al., 2019. On the applicability of registration uncertainty, in: 22<sup>nd</sup> International Conference on Medical Image Computing and Computer Assisted Intervention (MICCAI 2019), Springer. pp. 410–419.
- Meng, M., Feng, D., Bi, L., Kim, J., 2024. Correlation-aware Coarse-to-fine MLPs for Deformable Medical Image Registration, in: 2024 IEEE Conference on Computer Vision and Pattern Recognition (CVPR), pp. 9645–9654.
- Mok, T.C., Chung, A., 2021. Conditional deformable image registration with convolutional neural network, in: 24<sup>th</sup> International Conference on Medical Image Computing and Computer Assisted Intervention (MICCAI 2021), Springer. pp. 35–45.
- Niethammer, M., Kwitt, R., Vialard, F.X., 2019. Metric learning for image registration, in: 2019 IEEE Conference on Computer Vision and Pattern Recognition (CVPR), pp. 8463–8472.



- Ozaki, Y., Tanigaki, Y., Watanabe, S., Onishi, M., 2020. Multiobjective tree-structured parzen estimator for computationally expensive optimization problems, in: Proceedings of the 2020 genetic and evolutionary computation conference, pp. 533–541.
- Pace, D.F., Aylward, S.R., Niethammer, M., 2013. A locally adaptive regularization based on anisotropic diffusion for deformable image registration of sliding organs. *IEEE Trans. Med. Imag.* 32, 2114–2126.
- Risser, L., Vialard, F.X., Baluwala, H.Y., Schnabel, J.A., 2013. Piecewise-diffeomorphic image registration: Application to the motion estimation between 3D CT lung images with sliding conditions. *Medical Image Analysis* 17, 182–193.
- Rohlfing, T., 2011. Image similarity and tissue overlaps as surrogates for image registration accuracy: widely used but unreliable. *IEEE Trans. Med. Imag.* 31, 153–163.
- Ronneberger, O., Fischer, P., Brox, T., 2015. U-net: Convolutional networks for biomedical image segmentation, in: International Conference on Medical image computing and computer-assisted intervention, Springer. pp. 234–241.
- Selvaraju, R.R., Cogswell, M., Das, A., Vedantam, R., Parikh, D., Batra, D., 2017. Grad-cam: Visual explanations from deep networks via gradient-based localization, in: 2017 IEEE International Conference on Computer Vision (ICCV), pp. 618–626.
- Shen, Z., Vialard, F.X., Niethammer, M., 2019. Region-specific diffeomorphic metric mapping. *Advances in Neural Information Processing Systems* 32.
- Shi, J., He, Y., Kong, Y., Coatrieux, J.L., Shu, H., Yang, G., Li, S., 2022. XMorpher: Full transformer for deformable medical image registration via cross attention, in: 25<sup>th</sup> International Conference on Medical Image Computing and Computer Assisted Intervention (MICCAI 2022), Springer. pp. 217–226.
- Simpson, I.J., Schnabel, J.A., Groves, A.R., Andersson, J.L., Woolrich, M.W., 2012. Probabilistic inference of regularisation in non-rigid registration. *NeuroImage* 59, 2438–2451.
- Stefanescu, R., Pennec, X., Ayache, N., 2004. Grid powered nonlinear image registration with locally adaptive regularization. *Medical Image Analysis* 8, 325–342.
- Thirion, J.P., 1998. Image matching as a diffusion process: an analogy with Maxwell's demons. *Medical Image Analysis* 2, 243–260.
- Vercauteren, T., Pennec, X., Perchant, A., Ayache, N., 2009. Diffeomorphic demons: Efficient non-parametric image registration. *NeuroImage* 45, S61–S72.
- Vialard, F.X., Risser, L., 2014. Spatially-varying metric learning for diffeomorphic image registration: A variational framework, in: 17<sup>th</sup> International Conference on Medical Image Computing and Computer Assisted Intervention (MICCAI 2014), Springer. pp. 227–234.
- de Vos, B.D., et al., 2017. End-to-end unsupervised deformable image registration with a convolutional neural network, in: Deep learning in medical image analysis and multimodal learning for clinical decision support. Springer, pp. 204–212.
- Wang, Y., Qiu, H., Qin, C., 2023. Conditional Deformable Image Registration with Spatially-Variant and Adaptive Regularization. *arXiv preprint arXiv:2303.10700*.
- Wasserthal, J., Breit, H.C., Meyer, M.T., Pradella, M., Hinck, D., Sauter, A.W., Heye, T., Boll, D., Cyriac, J., Yang, S., et al., 2022. TotalSegmentator: robust segmentation of 104 anatomical structures in CT images. *arXiv preprint arXiv:2208.05868*.
- Watanabe, S., 2023. Tree-structured Parzen estimator: Understanding its algorithm components and their roles for better empirical performance. *arXiv preprint arXiv:2304.11127*.
- Woo, S., Debnath, S., Hu, R., Chen, X., Liu, Z., Kweon, I.S., Xie, S., 2023. Convnext v2: Co-designing and scaling convnets with masked autoencoders, in: 2023 IEEE Conference on Computer Vision and Pattern Recognition (CVPR), pp. 16133–16142.
- Zhai, X., Kolesnikov, A., Houlsby, N., Beyer, L., 2022. Scaling vision transformers, in: 2022 IEEE Conference on Computer Vision and Pattern Recognition (CVPR), pp. 12104–12113.
- Zhang, M., Fletcher, P.T., 2019. Fast diffeomorphic image registration via fourier-approximated lie algebras. *International Journal of Computer Vision* 127, 61–73.
- Zheng, J.Q., Wang, Z., Huang, B., Lim, N.H., Papież, B.W., 2024. Residual aligner-based network (ran): Motion-separable structure for coarse-to-fine discontinuous deformable registration. *Medical Image Analysis* 91, 103038.